The THESAN Project: ionizing escape fractions of reionization-era galaxies

by

Jessica Yuan-Chen Yeh

Submitted to the Department of Physics
in partial fulfillment of the requirements for the degree of

Bachelor of Science in Physics

at the

MASSACHUSETTS INSTITUTE OF TECHNOLOGY

May 2022

© Massachusetts Institute of Technology 2022. All rights reserved.

Author . . . .
Department of Physics
May 5, 2022

Certified by . . . .
Mark Vogelsberger
Associate Professor
Thesis Supervisor

Certified by . . . .
Aaron Smith
NASA Einstein Fellow
Thesis Supervisor

Accepted by . . . .
Deepto Chakrabarty
Associate Head of Physics

The THESAN Project: ionizing escape fractions of reionization-era galaxies

by

Jessica Yuan-Chen Yeh

Submitted to the Department of Physics
on May 5, 2022, in partial fulfillment of the
requirements for the degree of
Bachelor of Science in Physics

Abstract

A fundamental requirement for reionizing the Universe is that a sufficient fraction of the ionizing photons emitted by galaxies successfully escapes into the intergalactic medium. However, due to the scarcity of high-redshift observational data, the sources driving reionization remain uncertain. In this work we calculate the ionizing escape fractions ($f_{\rm esc}$) of reionization-era galaxies from the state-of-the-art THESAN simulations, which combine an accurate radiation-hydrodynamic solver (AREPO-RT) with the well-tested IllustrisTNG galaxy formation model to self-consistently simulate both small-scale galaxy physics and large-scale reionization throughout a large patch of the universe ($L_{\rm box} = 95.5\,{\rm cMpc}$). This allows the formation of numerous massive haloes ($M_{\rm halo} \gtrsim 10^{10}\,{\rm M}_\odot$), which are often statistically underrepresented in previous studies but are believed to be important to achieving rapid reionization. We find that low-mass galaxies ($M_{\rm stars} \lesssim 10^7\,{\rm M}_\odot$) are the main drivers of reionization above $z \gtrsim 7$, while high-mass galaxies ($M_{\rm stars} \gtrsim 10^8\,{\rm M}_\odot$) dominate the escaped ionizing photon budget at lower redshifts. We find a strong dependence of $f_{\rm esc}$ on the effective star-formation rate (SFR) surface density defined as the SFR per gas mass per escape area. The variation in halo escape fractions decreases for higher mass haloes, which can be understood from the more settled galactic structure, SFR stability, and fraction of sightlines within each halo significantly contributing to the escaped flux. We show that dust is capable of reducing the escape fractions of massive galaxies, but the impact on the global $f_{\rm esc}$ depends on the dust model. Finally, AGN are unimportant for reionization in THESAN and their escape fractions are lower than stellar ones due to being located near the centres of galaxies gravitational potential wells.

Thesis Supervisor: Mark Vogelsberger
Title: Associate Professor

Thesis Supervisor: Aaron Smith
Title: NASA Einstein Fellow

Acknowledgments

First and foremost, I would like to thank my supervisor Dr. Aaron Smith for his guidance and support, his physical insights into this project, and the hours he spent teaching me how to code and how to write papers. This thesis would not be possible without his patience and confidence in me.

I am also thankful to Prof. Mark Vogelsberger for giving me the chance to work in his group, for his graduate school advice, and for being a great instructor in 8.04 (Quantum Physics I), which is my first advanced physics class at MIT.

I have learned so much about physics and how to do research during my time in the Vogelsberger group. I am grateful for the comments and feedback from all the group members and collaborators: Josh Borrow, Enrico Garaldi, Rahul Kannan, Hui Li, Meredith Neyer, Stephanie O'Neil, and Clara Xu.

I would like to extend my gratitude to friends and pset partners at MIT and abroad. Their constant support and company, either in-person or virtual, have made my four years at MIT an unforgettable journey. I also want to thank Prof. Netta Engelhardt, Prof. Vladan Vuletic, Prof. Phiala Shanahan, Prof. Liang Fu, Prof. Xiao-Gang Wen, Prof. Max Metlitski, Prof. Salvatore Vitale, and Prof. Scott Hughes for their amazing physics lectures and influence on me as a future physicist.

Lastly, I owe the greatest debt of gratitude to my family for their endless love from 8000 miles away. Even though they think my research is to perform "dark magic" and look for the wormholes in the Universe, they still always have unwavering faith in me to achieve the impossible.

Contents

List of Figures

List of Tables

Chapter 1

Introduction

The formation of the first stars and galaxies marks the end of the cosmic dark ages and the beginning of the Epoch of Reionization (EoR; Bromm and Yoshida, 2011; Loeb and Furlanetto, 2013). Lyman continuum (LyC; photon energy $h\nu > 13.6\,\mathrm{eV}$) radiation capable of ionizing atomic hydrogen was emitted by a growing number of sources, including young, hot massive stars. These photons primarily interacted with the surrounding interstellar medium (ISM), although a significant fraction successfully traversed through the circumgalactic medium (CGM) of their host galaxies to emerge into the vast intergalactic medium (IGM). The result was to transform the originally cold and neutral atoms into a hot plasma through photo-ionization and photo-heating (Madau et al., 1999; Barkana and Loeb, 2001). However, the complex nature of this last major phase transition of the Universe still presents many important unanswered questions. For instance, what are the main sources and sinks of ionizing photons in this period, what determines the morphology and coalescence timeline of ionized bubbles, and how do these translate to observational signatures for current and upcoming facilities? To answer these questions, significant effort has been made to better understand the ionizing source emissivity, either through inferred measurements or theoretical modelling (e.g. Robertson et al., 2010; Wise, 2019; Eide et al., 2020). It is widely believed that star-forming galaxies are the primary sources of reionization (Haardt and Madau, 2012; Faucher-Giguère, 2020). Throughout this work we focus on the escape fraction f_{esc}, which we define as the ratio between the number of photons that escape galaxies to reach the IGM and the number of photons intrinsically emitted. As galaxy formation constraints improve, e.g. for stellar population synthesis modelling and stellar-to-halo mass relations, the escape fractions directly dictate the amount of radiation galaxies can contribute to reionization. However, the majority of the measured values of escape fractions to date are not high enough to fully reionize the Universe (Finkelstein et al., 2012; Robertson et al., 2013), and thus expose our lack of a complete understanding of reionization. In the following we briefly summarize observational and theoretical approaches that have been explored to rectify this inconsistency.

There are at least two major challenges when determining $f_{\rm esc}$ observationally. Firstly, the high opacity of the intervening neutral IGM at high redshifts means that very limited observational data is available at present. In fact, certain properties such as the intrinsic LyC flux may never be directly observable, while other measurements such as Lyman-α (Lyα) absorption spectra become highly saturated. Secondly, it has been shown that $f_{\rm esc}$ has large sightline-to-sightline variability (Cen and Kimm, 2015). In other words, individual observations may not be able to yield a representative picture and a large number of galaxies are needed to provide robust constraints. Despite these difficulties, several observations have been made by measuring the leakage of LyC photons, but due to detection biases most of which originate from starburst galaxies at $z \lesssim 3$, and almost all results indicate low $f_{\rm esc}$. For example, $f_{\rm esc}$ of a few per cent at $z \approx 1$ were detected in star-forming galaxies by Bridge et al. (2010), Siana et al. (2010), and Rutkowski et al. (2016). More optimistically, averages of $f_{\rm esc} \sim 10\%$ at $z \approx 3$ were found by Nestor et al. (2013), Grazian et al. (2017), Japelj et al. (2017), Steidel et al. (2018), and Pahl et al. (2021). Recently the Low-Redshift Lyman Continuum Survey (LzLCS) measured a median $f_{\rm esc}$ of 4% from galaxies at $z = 0.2$–0.4 (Flury et al., 2022; Saldana-Lopez et al., 2022). Only a few galaxies with uncharacteristically high $f_{\rm esc}$ have been reported (Vanzella et al., 2018; Izotov et al., 2018; Rivera-Thorsen et al., 2019). Looking forward, we expect more data to become available from upcoming facilities, including probing the faint and bright ends of the UV luminosity function with the *James Webb Space Telescope* (*JWST*) and

Nancy Grace Roman Space Telescope (*NGRST*), as well as 21 cm cosmology measurements at high-redshift with the Low-Frequency Array (LOFAR), Hydrogen Epoch of Reionization Array (HERA), and Square Kilometer Array (SKA).

The uncertainty in determining escape fractions propagates to different predictions for the global reionization history. In particular, if the dominant photon sources are low-mass galaxies ($M_{\rm halo} \lesssim 10^9\,{\rm M}_\odot$), then reionization will have started earlier (e.g. Finkelstein et al., 2019), reaching an IGM ionized volume filling fraction of 0.5 at $z = 9$. On the other hand, late reionization is favoured if massive galaxies ($M_{\rm halo} \gtrsim 10^{10}\,{\rm M}_\odot$) prevail, potentially delaying the midpoint of reionization to around $z = 6.8$ (e.g. Naidu et al., 2020). In this scenario reionization proceeds significantly more rapidly than early reionization models, especially at the tail end (Robertson et al., 2015). Recently, late reionization has gained popularity, increasing the importance of studying $f_{\rm esc}$ from massive galaxies. This is supported by the measurement of a much lower optical depth for electron scattering of cosmic microwave background (CMB) photons than previous studies (Planck Collaboration et al., 2020), a rapid decrease of the observed Lyα emission (Schenker et al., 2014; Mason et al., 2019), and the damping wing absorption on the spectrum of high-redshift quasars (Davies et al., 2018). Collectively, the observations suggest that reionization was nearly complete by $z \approx 6$ (McGreer et al., 2015) with large islands of neutral hydrogen remaining in underdense regions below $z \approx 5.5$ (Kulkarni et al., 2019).

The difficulty of obtaining statistically significant data at high-redshift ($z \gtrsim 6$) makes theoretical modelling critical in the study of the EoR. However, determining $f_{\rm esc}$ with numerical simulations is also an extremely complicated problem since the details can depend on the models used for galaxy formation, feedback recipes, multiphase ISM, and dust physics. Some early studies based on cosmological simulations predict that escape fractions are correlated with the galaxy mass (Gnedin et al., 2008; Wise and Cen, 2009) while some suggest the opposite trend (Yajima et al., 2011). On the contrary, a combination of studies from more recent radiation-hydrodynamic or post-processed radiative transfer simulations indicate a more complicated dependence of $f_{\rm esc}$ on halo mass: $f_{\rm esc}$ decreases with halo mass for haloes up to $10^9\,{\rm M}_\odot$

(Paardekooper et al., 2015; Xu et al., 2016) with high $f_{\rm esc}$ in faint galaxies (Kimm et al., 2017). Ma et al. (2020) found the $f_{\rm esc}$ increases with halo mass for $M_{\rm halo} = 10^8$–$10^{9.5}\,{\rm M}_\odot$ and decreases for more massive haloes at $\gtrsim 10^{11}\,{\rm M}_\odot$. Predicted $f_{\rm esc}$ from a wide range of hydrodynamical simulations have been found to be from a few percent to thirty percent (Ma et al., 2015; Paardekooper et al., 2015; Xu et al., 2016; Rosdahl et al., 2018; Trebitsch et al., 2018; Ma et al., 2020, 2021). The potential boost in $f_{\rm esc}$ due to binary stars has also been explored (Ma et al., 2016, 2022). However, due to the high computational cost associated with large-volume simulations, most above-mentioned simulations either only have haloes with $M_{\rm halo}$ up to $10^9\,{\rm M}_\odot$ or do not have enough statistics in massive haloes ($M_{\rm halo} \gtrsim 10^{11}\,{\rm M}_\odot$) and therefore cannot provide a complete picture of the role of more massive galaxies in the reionization process.

In this work, we provide a detailed study of ionizing escape fraction statistics and the underlying properties of the galaxies that contribute to reionization by using the THESAN simulations (Kannan et al., 2022; Garaldi et al., 2022; Smith et al., 2022). The strength of THESAN is the significantly-expanded range of physical processes, based on combining the IllustrisTNG galaxy formation model with a self-consistent on-the-fly treatment of radiation with AREPO-RT, while simulating a large volume of the Universe at state-of-the-art resolution. As a result, THESAN successfully produces realistic galaxies that match important physical quantities relevant to the EoR.

The thesis is organized as follows. In Chapter 2, we describe the THESAN simulations and radiative transfer analysis methodology. In Chapter 3, we present insights into the global production and escape statistics of LyC photons. In Chapter 4, we explore the dependence on halo properties and variation across galaxy populations. In Chapter 5, we discuss the halo-to-halo variations in escape fractions and characterize the anisotropic behaviour across sightlines from individual haloes. In Chapter 6, we discuss several important caveats, including the sub-resolution modelling, dust pre-absorption of ionizing photons, and contribution of active galactic nuclei (AGN). Finally, in Chapter 7, we provide a summary of our main results and possible future investigations.

Chapter 2

Methods

We briefly describe the THESAN reionization simulations in Chapter 2.1, focusing on aspects of the model that are particularly relevant for our study of escape fractions in the EoR. In Chapter 2.2 we discuss the halo selection and completeness of our escape fraction catalogues. Finally, in Chapter 2.3 we summarize the outcomes of the Monte Carlo radiative transfer (MCRT) calculations employed to obtain $f_{\rm esc}$ from galaxies extracted from the THESAN simulation.

2.1 THESAN simulations

The THESAN project is a suite of large-volume radiation-magneto-hydrodynamic simulations that self-consistently model the hydrogen reionization process and the resolved properties of the sources (galaxies and AGN) responsible for it. The simulations were performed with AREPO-RT (Kannan et al., 2019), a radiation-hydrodynamic extension of the moving mesh code AREPO (Springel, 2010; Weinberger et al., 2020), which solves the fluid equations on an unstructured Voronoi mesh that is allowed to move along with the fluid flow for an accurate quasi-Lagrangian treatment of cosmological gas flows. Gravitational forces are calculated using a hybrid Tree-PM approach, which splits the force into a short-range force that is computed using an oct-tree algorithm (Barnes and Hut, 1986) and a long-range force, estimated using a particle mesh approach.

Radiation fields are modelled using a moment based approach that solves the zeroth and first moments of the radiative transfer equation (Rybicki and Lightman, 1986), coupled with the M1 closure relation, that approximates the Eddington tensor based on the local properties of each cell (Levermore, 1984). They are coupled to the gas via a non-equilibrium thermo-chemistry module, which self-consistently calculates the ionization states and cooling rates from hydrogen and helium, while also including equilibrium metal cooling and Compton cooling of the CMB (Kannan et al., 2019). Both stars and AGN act as sources of radiation, with the spectral energy distribution of stars taken from the Binary Population and Spectral Synthesis models (BPASS; Eldridge et al., 2017). The AGN radiation output is scaled linearly with the mass accretion rate with a radiation conversion efficiency of 0.2 (Weinberger et al., 2018) and a Lusso et al. (2015) parametrization for the shape of its spectrum.

The prescriptions for processes happening below the resolution limit of the simulations, such as star and black hole formation and feedback and metal production and enrichment, are taken from the IllustrisTNG model (Weinberger et al., 2017; Springel et al., 2018; Pillepich et al., 2018b,a; Naiman et al., 2018; Marinacci et al., 2018; Nelson et al., 2018, 2019; Pillepich et al., 2019). The model is augmented with a scalar dust model that tracks the production, growth, and destruction of dust using the formalism outlined in (McKinnon et al., 2017). An additional birth cloud escape fraction parameter, $f_{\rm esc}^{\rm cloud} = 0.37$, is added to mimic the absorption of LyC photons happening below the resolution scale of the simulation. The parameter is tuned such that the simulation reproduces a realistic late-reionization history (Kannan et al., 2022), which matches the observed neutral fraction evolution in the Universe (Greig et al., 2017).

All THESAN simulations follow the evolution of a cubic patch of the universe with linear comoving size $L_{\rm box} = 95.5\,{\rm cMpc}$, and utilize variance-suppressed initial conditions (Angulo and Pontzen, 2016). We employ a Planck Collaboration et al. (2016) cosmology (`TT,TE,EE+lowP+lensing+BAO+JLA+H`$_0$ dataset), i.e. $H_0 = 100\,h\,{\rm km\,s^{-1}Mpc^{-1}}$ with $h = 0.6774$, $\Omega_{\rm m} = 0.3089$, $\Omega_\Lambda = 0.6911$, $\Omega_{\rm b} = 0.0486$, $\sigma_8 = 0.8159$, and $n_s = 0.9667$, where all symbols have their usual meanings. In this work we focus on the highest resolution THESAN-1 simulation, which has a dark matter mass resolution of $3.12 \times 10^6\,\mathrm{M}_\odot$ and a baryonic mass resolution of $5.82 \times 10^6\,\mathrm{M}_\odot$. The gravitational forces are softened on scales of 2.2 ckpc with the smallest cell sizes reaching 10 pc. This allows us to model atomic cooling haloes throughout the entire simulation volume.

2.2 Halo selection

The THESAN simulation uses the friends-of-friends (FoF; Springel, 2005) algorithm as implemented on-the-fly in AREPO to group dark matter particles into resolved structures along with their associated gas and star particles. The SUBFIND algorithm as first described in Springel et al. (2001) is then used to identify gravitationally bound sub-structures, which form the basis of the haloes hosting the galaxies referred to throughout this work. However, for clarity we define M_{halo} to be the halo mass within the radius at which the average density reaches 200 times the density of the universe, M_{200}. Similarly, we adopt this same definition for M_{stars} as the stellar mass within R_{200}, the star formation rate (SFR) as the sum of the instantaneous SFRs of gas particles within R_{200}, and the virial radius, i.e. $R_{\mathrm{vir}} \equiv R_{200}$. These definitions are chosen to ensure a consistent accounting of properties contributing to the escape fraction calculations.

At this point we select a sub-sample of haloes from the full catalogues that contain at least one star and four gas cells within the virial radius. On a practical level, these criteria are chosen to ensure Voronoi mesh reconstructions in ray-tracing are robust and therefore reasonable escape fractions can be defined. Although we do not claim all selected haloes are well resolved, our criteria maximize the completeness in halo selection and thus provide a less biased transition from selected haloes to non-selected haloes in the catalogue. We emphasize that any requirement on the number of gas or star particles induces selection biases, which in the context of the IllustrisTNG galaxy formation model arise from stochastic star formation leading to characteristically bursty star formation histories increasing the variation at the low mass end of the stellar-to-halo mass relation (Genel et al., 2019; Iyer et al., 2020).

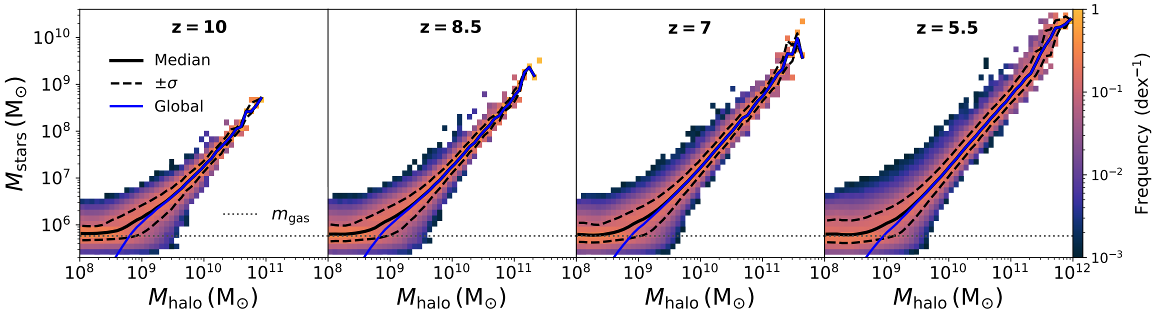

Figure 2-1: The stellar-to-halo mass relation for all stars within R_{200} for all selected haloes at $z = \{10, 8.5, 7, 5.5\}$. The black solid curves show the median while the black dashed curves show the 16th and 84th percentiles of the selected data. The blue curves show the average stellar mass from the full halo catalogue. The mismatch between the selected haloes and the full catalogue comes from the fact that only haloes with at least one star particle are selected. The flattening at the low-mass end is due to the baryonic mass resolution of $m_{\rm gas} \approx 5.8 \times 10^5\,{\rm M}_\odot$ from the THESAN simulation, as indicated by the gray dotted lines. The coloured histogram illustrates the full distribution with each bin normalized by the number of haloes in the given halo mass range, i.e. the following equation holds: $\int p(M_{\rm star}|M_{\rm halo})\,{\rm d}\log M_{\rm star} = 1$.

In Fig. 2-1 we show the stellar-to-halo mass relation for our selected sample of haloes at $z = \{10, 8.5, 7, 5.5\}$. The above selection criteria result in a wide range of haloes from $M_{\rm halo} = 10^8$–$10^{12}\,{\rm M}_\odot$. Haloes below $10^8\,{\rm M}_\odot$ are not well-resolved in the THESAN simulation, but these are only expected to be important during the earliest stages of reionization (Paardekooper et al., 2013; Wise et al., 2014). The stellar-to-halo mass relation in THESAN is in agreement with current observational estimates (Kannan et al., 2022). In Fig. 2-2 we show that our selection criteria result in a very high completeness for haloes more massive than $10^9\,{\rm M}_\odot$. That is, our selection covers most of the haloes with $M_{\rm halo} > 10^9\,{\rm M}_\odot$ in the catalogue. Specifically, near the midpoint of reionization at $z \approx 7.67$ we achieve greater than $\{10, 50, 90\}\%$ cumulative completeness at halo masses of $M_{\rm halo} \approx \{1.0, 3.2, 12\} \times 10^8\,{\rm M}_\odot$.

2.3 Post-processing radiative transfer

As alluded to above, we define the escape fraction of a halo as the ratio between the number of ionizing photons that escape and are intrinsically emitted from all sources

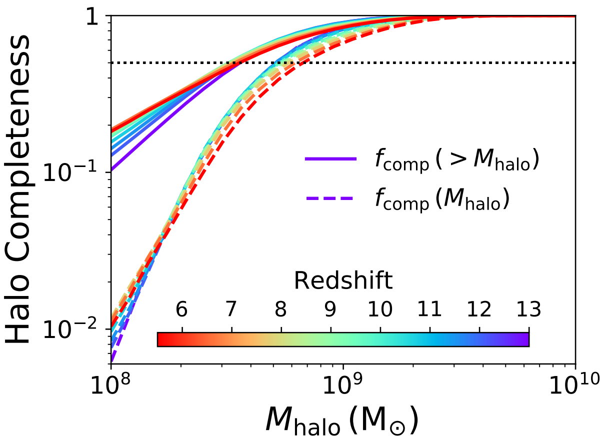

Figure 2-2: The completeness is defined as the fraction of selected haloes and haloes in the catalogue. The solid curves show the cumulative completeness for all haloes above a given mass and the dashed curves show the completeness at a specific mass at several different redshifts. The cumulative completeness exceeds 90% when $M_{\rm halo} \gtrsim 10^9\,{\rm M}_\odot$ for nearly all redshifts, and reach 50% when $M_{\rm halo} \approx 3 \times 10^8\,{\rm M}_\odot$ as shown by the black dotted line.

within the virial radius, i.e.

$$f_{\rm esc} \equiv \frac{\dot{N}_{\rm esc}}{\dot{N}_{\rm int}}\,. \tag{2.1}$$

The escape fractions for star particles outside the virial radius of any halo are assumed to be maximal (recall that $f_{\rm esc}^{\rm cloud} = 0.37$ from the birth cloud) as these directly contribute to reionizing the IGM. The same applies for stars in haloes with fewer than four gas particles (non-selected haloes), which do not possess enough opacity to lead to a significant amount of photon absorption in agreement with calculations of $f_{\rm esc}$ in low-mass haloes. The intrinsic photon rate for each subhalo (including stars outside R_{200}) is provided in the Lyα emission catalogue described in Smith et al. (2022), which is calculated from the Binary Population and Spectral Synthesis models (BPASS version 2.2.1; Eldridge et al., 2017) with a Chabrier IMF (Chabrier, 2003). The photon rates within R_{200} are calculated from the same exact age–metallicity tables as part of the radiative transfer calculations within the Cosmic Lyα Transfer (COLT) code (Smith et al., 2015, 2019). This ensures consistent results for global properties when accounting for all ionizing sources. The details of the photo-ionization physics and MCRT implementation are described in Smith et al. (2021), and we only summarize the main features and differences here. Most importantly, we perform passive RT as our goal is to obtain escape fraction statistics based on the on-the-fly ionization states in the THESAN simulation rather than recompute new ones based on the assumption of photo-ionization equilibrium. Our escape fraction calculations employ 10^5 photon packets for haloes with fewer than 10 star particles, while the photon count increases linearly with the number of star particles up to a maximum of 10^7 packets for well-converged statistics. Similar to THESAN, we model the multi-frequency ionizing radiation field in three bands, HI, HeI, and HeII with energy edges of $[13.6, 24.59, 54.42, \infty)\,\mathrm{eV}$. We employ continuous absorption algorithms for the treatment of photoionization, with frequency dependent cross-sections taken from Verner et al. (1996). The emission direction is isotropic and the initial position corresponds to the location of the star. We employ native ray-tracing through the Voronoi tessellation.

Dust absorption has a non-negligible effect on the escape of LyC photons and has been discussed in previous studies (see e.g. Puglisi et al., 2016; Tacchella et al., 2018, 2021). THESAN integrates the production and destruction of dust based on the empirical model of McKinnon et al. (2017), and treats dust as a property of the gas resolution elements. As in Smith et al. (2021), we can isolate the pre-absorption of ionizing photons by dust, according to

$$f_{\mathrm{abs}} \equiv \ell^{-1} \int_0^{\ell} \frac{k_{\mathrm{a,d}}}{k_{\mathrm{a}}} e^{-k_{\mathrm{a}}\ell'} \mathrm{d}\ell' \,, \tag{2.2}$$

where $k_{\mathrm{a,d}}$ and k_{a} denote the dust and total absorption coefficients along the path integration of length ℓ. The absorption by hydrogen and helium can also be calculated in a similar way by replacing $k_{\mathrm{a,d}}$ with $k_{\mathrm{i}} = n_{\mathrm{i}}\sigma_{\mathrm{i}},\ i \in \{\mathrm{HI}, \mathrm{HeI}, \mathrm{HeII}\}$. We note that it is challenging to resolve dust in ionized HII regions with the resolution of the THESAN simulation because of the ISM and feedback models. Hence, the fiducial MCRT calculation in this work assumes a no-dust scenario, and we postpone a more detailed estimation of the effect of dust absorption to Chapter 6. Finally, the ray-tracing procedure also allows us to conveniently track the average distance to absorption, defined as:

$$\langle \ell \rangle \equiv \ell^{-1} \int_0^{\ell} \ell' e^{-k_{\rm a}\ell'} {\rm d}\ell' \,, \tag{2.3}$$

which provides complementary information about the ionization and dust absorption of photons that we explore in later chapters.

Chapter 3

Global statistics

3.1 Large-scale structure

In Fig. 3-1, we present a visualization of the spatial distribution of the volume-weighted HII fraction $\langle x_{\rm HII} \rangle$, gas overdensity $\delta \equiv \rho/\bar{\rho} - 1$, escaped ionizing photon rate densities $\rho_{\rm esc}$, and LyC escape fractions $f_{\rm esc}$ across a $95.5 \times 95.5 \times 9.55\,{\rm cMpc}^3$ sub-volume at redshifts $z = \{10, 8.5, 7, 5.5\}$. $\rho_{\rm esc}$ and $f_{\rm esc}$ are calculated by dividing the sub-volume into a grid and summing up the contributing haloes in each pixel region. We also apply a Gaussian filter over the grid to smooth out the halo distribution. The similarity in morphology among the four quantities can be readily seen. At $z \gtrsim 8$, the reionization of hydrogen corresponds with the highest overdensity regions, which are the earliest sites of galaxy formation and are thus capable of providing the most intrinsic and escaped ionizing photons at these epochs. The HII regions then expand and fill the entire simulation volume at the end of the simulation at $z = 5.5$ (bottom panel). Regions with high $\rho_{\rm esc}$ and $f_{\rm esc}$ also generally align with the high overdensity regions at higher redshifts, and they expand into the nearby regions as time increases. At the end, even regions with overdensity less than zero (under-densities) can have relatively high $\rho_{\rm esc}$ and $f_{\rm esc}$. This emphasizes the important role environment plays during reionization, and neighborhoods without significant star formation can be externally reionized via the ionizing sources nearby.

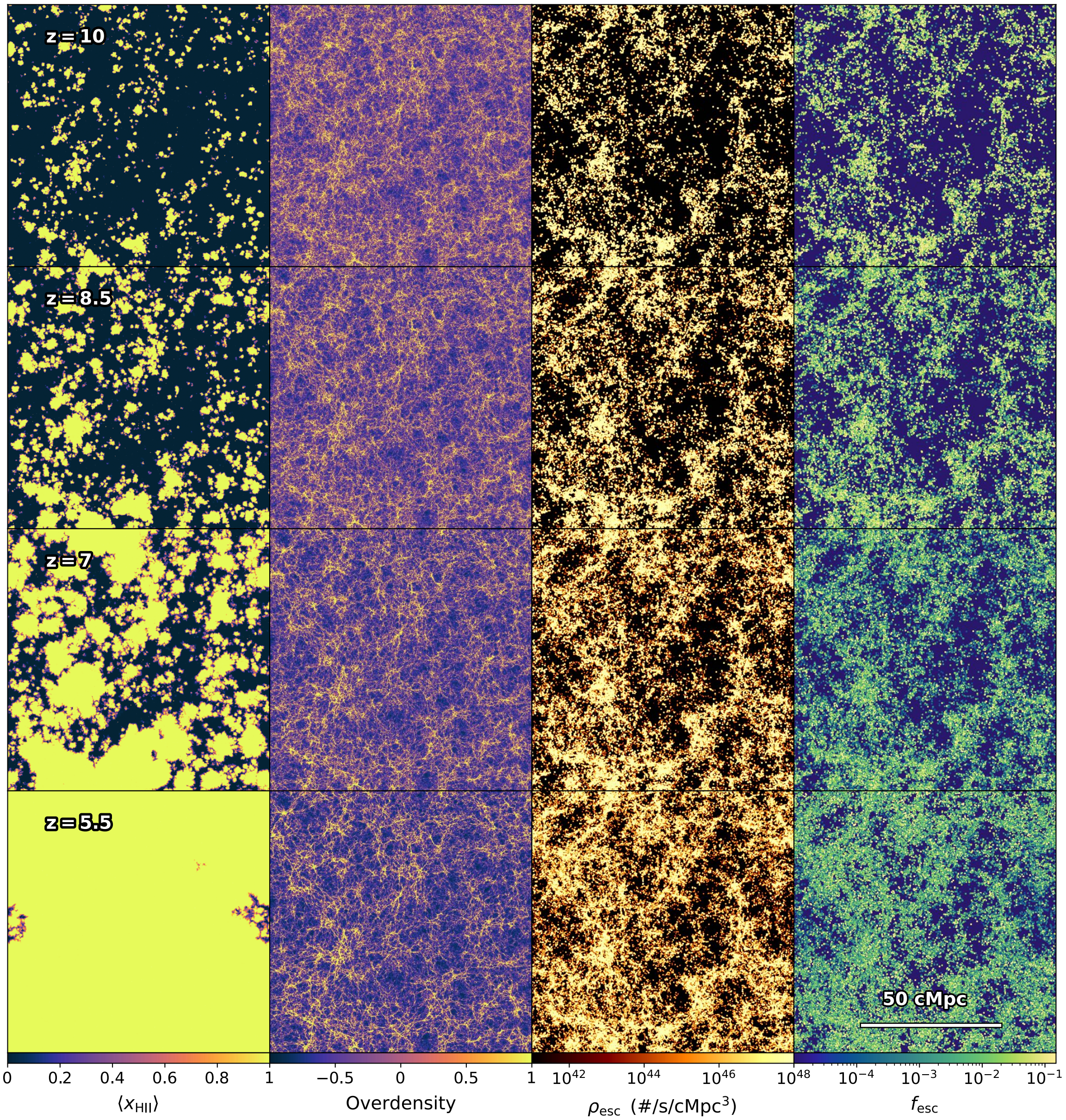

Figure 3-1: *Left to right:* Visualization of the spatial distribution of the HII fraction $\langle x_{\mathrm{HII}} \rangle$, gas overdensity $\delta \equiv \rho/\bar{\rho} - 1$, escaped ionizing photon rate densities ρ_{esc}, and LyC escape fractions f_{esc}, covering the same $95.5 \times 95.5 \times 9.55\,\mathrm{cMpc}^3$ sub-volume at redshifts $z = \{10, 8.5, 7, 5.5\}$, from top to bottom. The similarity in morphology among these quantities is striking, and indicates that environment also influences the production and escape of ionizing photons in the EoR.

3.2 Redshift evolution

We next present quantitative results for the global statistics, which are critical for understanding the evolution of the IGM ionized volume fraction and therefore the reionization history (Madau et al., 1999). In the left panels of Fig. 3-2 we show the global escape fraction (thick black curves) defined as $\langle f_\text{esc} \rangle \equiv \sum \dot{N}_\text{esc} / \sum \dot{N}_\text{int}$, where the summations are over all photon sources. In particular, this includes all resolved subhaloes with MCRT calculations but also all stars outside the virial radius of any halo assuming maximal escape fractions. In fact, the plotted range corresponds to $f_\text{esc}^\text{cloud} = 0.37$ for consistency with the birth cloud value used in THESAN to match available constraints on the observed reionization history. To reduce distracting numerical fluctuations, we have applied a Savitzky-Golay smoothing filter to all values. To show the dependence on the halo mass, in the upper panels we also calculate the global contributions from sources split into five different mass ranges defined by the following thresholds: $M_\text{halo} \in (0, 10^8, 10^9, 10^{10}, 10^{11}, \infty)\,\text{M}_\odot$. Likewise, in the lower panels we separate the dependence on the stellar mass in the following ranges: $M_\text{stars} \in (0, 10^6, 10^7, 10^8, 10^9, \infty)\,\text{M}_\odot$. In comparison to previous similar studies (e.g. Paardekooper et al., 2015; Rosdahl et al., 2018), our larger simulation volume provides us with significantly more data for massive galaxies. For reference, we also include the result from Rosdahl et al. (2018) as shown with the blue dashed curve, specifically the luminosity-weighted mean over the last 100 Myr (i.e. shown as $f_\text{esc,100}$ from the binary SED model in their Fig. 13). Lastly, we compare our post-processing escape fractions to the effective escape fractions f_esc^eff (black dashed lines) calculated in Sec. 3.3 of Kannan et al. (2022) using the equations outlined in Madau (2017). Our results show that the effective escape fractions f_esc^eff overestimate the escape fractions before $z \approx 6$. In addition, our ray-tracing RT approach results in a redshift-dependent, galaxy-mass dependent f_esc, which is not seen in the zeroth order estimation of f_esc^eff.

In the right panels we show the total intrinsic (dashed curves) and escaped (solid curves) cosmic photon rate densities, i.e. normalized by the volume of the THESAN simulation. The intrinsic photon rate density rises from $\sim 10^{51}\,\text{photons s}^{-1}\,\text{cMpc}^{-3}$

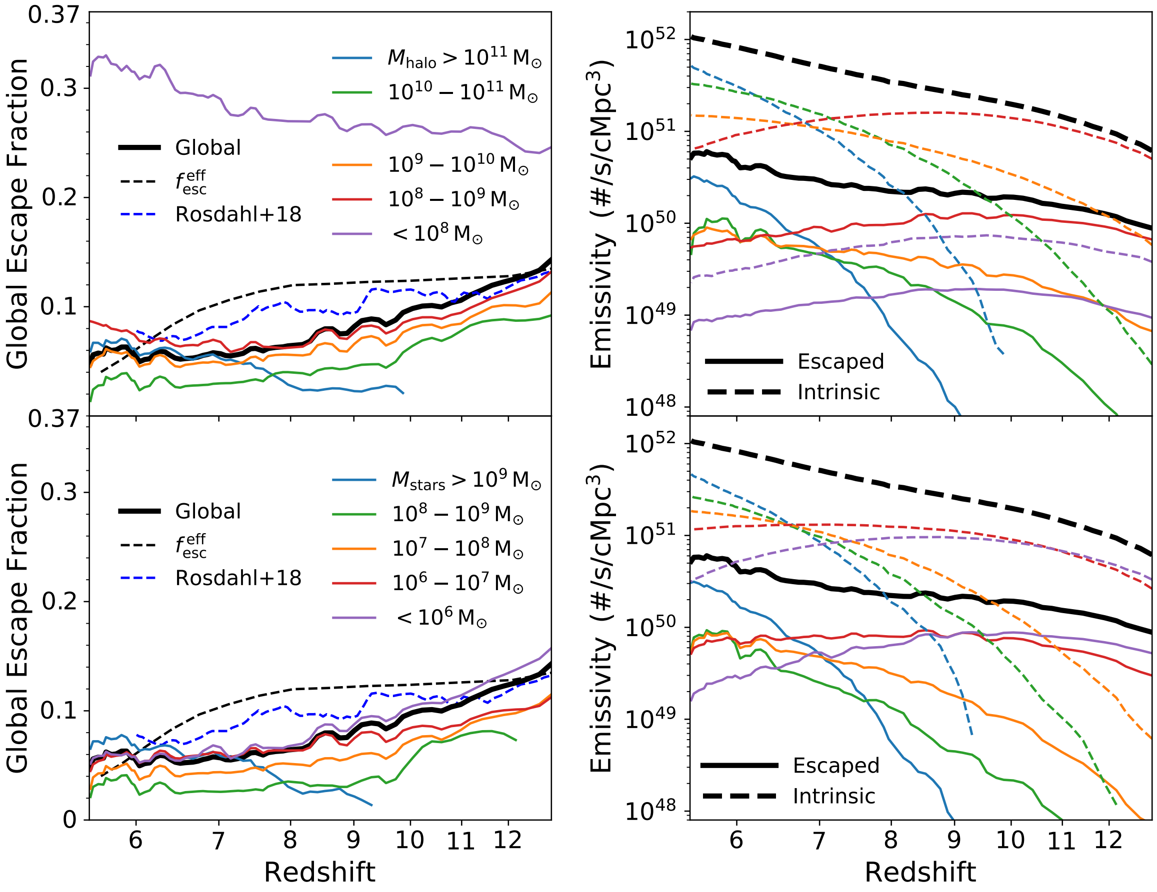

Figure 3-2: *Left:* Global photon rate weighted escape fractions $\langle f_{\rm esc} \rangle \equiv \sum \dot{N}_{\rm esc} / \sum \dot{N}_{\rm int}$ as a function of redshift (thick black curves). This contains all photon sources in the simulated volume, including all resolved haloes and a small fraction of unassigned star particles. The overall escaped photon rates are obtained using the $f_{\rm esc}$ calculated by COLT for all selected haloes and assuming maximal escape $f_{\rm esc}^{\rm cloud} = 0.37$ for the remaining sources. We also show global escape fractions for haloes in five different halo (upper panels) and stellar (lower panels) mass ranges (coloured curves), which reflect the nontrivial mass dependence with redshift. The lowest-mass haloes have lower completeness for stars within the virial radius and thus have maximal escape properties. Overall, the weighted-$f_{\rm esc}$ decreases with increasing halo mass except for the most massive haloes (either $M_{\rm halo} > 10^{11}\,{\rm M}_\odot$ or $M_{\rm stars} > 10^{9}\,{\rm M}_\odot$). The black dashed curve shows the effective escape fraction $f_{\rm esc}^{\rm eff}$ calculated from the equations in Madau (2017). For reference we also include the result from Rosdahl et al. (2018) (blue dashed curves). *Right*: Global intrinsic (solid) and escaped (dashed) photon rate densities as functions of redshift (thick black curves), also plotted with the same mass bin ranges (coloured curves). The emissivity evolution is mainly due to the formation of massive galaxies at lower redshifts, with a slightly flattened slope when going from intrinsic to escaped values. The halo and stellar mass dependence clearly show that massive haloes become the dominant photon sources by $z \approx 7$.

at $z = 13$ to $\sim 10^{52}$ photons $\mathrm{s}^{-1}\,\mathrm{cMpc}^{-3}$ at $z = 5.5$, while the escaped photon rate density has a slightly flatter evolution over the same period of time. In fact, there is a clear decrease in the global effective escape fraction from $\approx 15\%$ to $\approx 5\%$, with varying behaviour across the individual halo and stellar mass ranges. Notably, in our model the escape fractions of the lowest-mass unresolved haloes ($< 10^8\,\mathrm{M}_\odot$) are close to the maximal values but have a small contribution to reionization due to their low intrinsic photon rates. As reionization progresses the emissivity transitions from being dominated by atomic cooling haloes ($M_{\text{halo}} \approx 10^8$–$10^9\,\mathrm{M}_\odot$) to more massive haloes. The suppressed star formation in this mass range is likely due to photoheating feedback by the reionization process itself, which reduces the accretion of gas onto smaller haloes (Gnedin, 2014; Dawoodbhoy et al., 2018; Wu et al., 2019).

3.3 Importance of halo mass

The increasing photon rate densities can also be understood by considering the redshift evolution of the halo and stellar mass distributions towards more massive objects. Conceptually, the intrinsic luminosity of a galaxy is roughly proportional to its star formation rate, which is correlated with the halo and stellar mass. In Fig. 3-3 we show the global intrinsic (top) and escaped (middle) photon rate density distributions along with the escape fraction (bottom) as functions of halo mass (10^8–$10^{12}\,\mathrm{M}_\odot$) for several different redshift bins across the range $z = 5.5$–13 as indicated in the colour bar. Data in the same redshift bins are combined to improve the statistics. The solid curves are the underlying mass distributions while the dashed curves represent cumulative values from the massive end. At nearly all redshifts the low mass peak coincides with the range of marginally resolved haloes in the simulation $M_{\text{halo}} \approx 10^8$–$10^9\,\mathrm{M}_\odot$, i.e. haloes below this have low stellar occupation fractions so do not emit significant ionizing radiation. The low-mass bump gradually becomes less dominant with time as more massive haloes start to dominate the production budget, which indicates that the increasing photon rate densities mainly arise from the formation of more massive galaxies at lower redshifts. We directly demonstrate the importance of

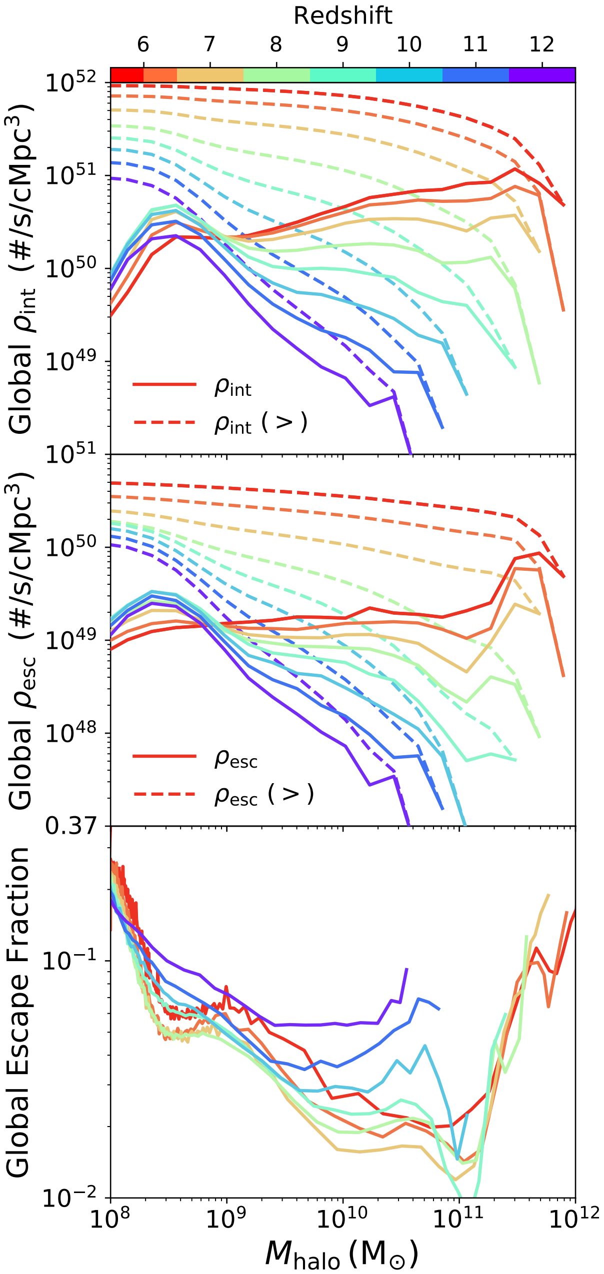

Figure 3-3: The distribution of global intrinsic (top) and escaped (middle) photon rate densities along with the escape fraction (bottom) as functions of halo mass for several redshift ranges covering $z = 5.5$–13 as indicated in the colour bar. The solid curves are mass distributions while the dashed curves are cumulative values from the massive end. Haloes at the low mass end ($M_{\rm halo} \lesssim 10^9\,{\rm M}_\odot$) are less resolved while more massive ones ($M_{\rm halo} \gtrsim 10^{11}\,{\rm M}_\odot$) only form at lower redshifts given the moderate volume of the THESAN simulation. Lower-mass haloes are the main intrinsic and escaped photon sources at $z \gtrsim 8$ while higher-mass haloes become dominant at lower redshifts. The most massive haloes are especially strong sources of escaped photons at $z \lesssim 7$ as indicated by the noticeable peak in the middle panel and upturn in the escape fraction shown in the bottom panel.

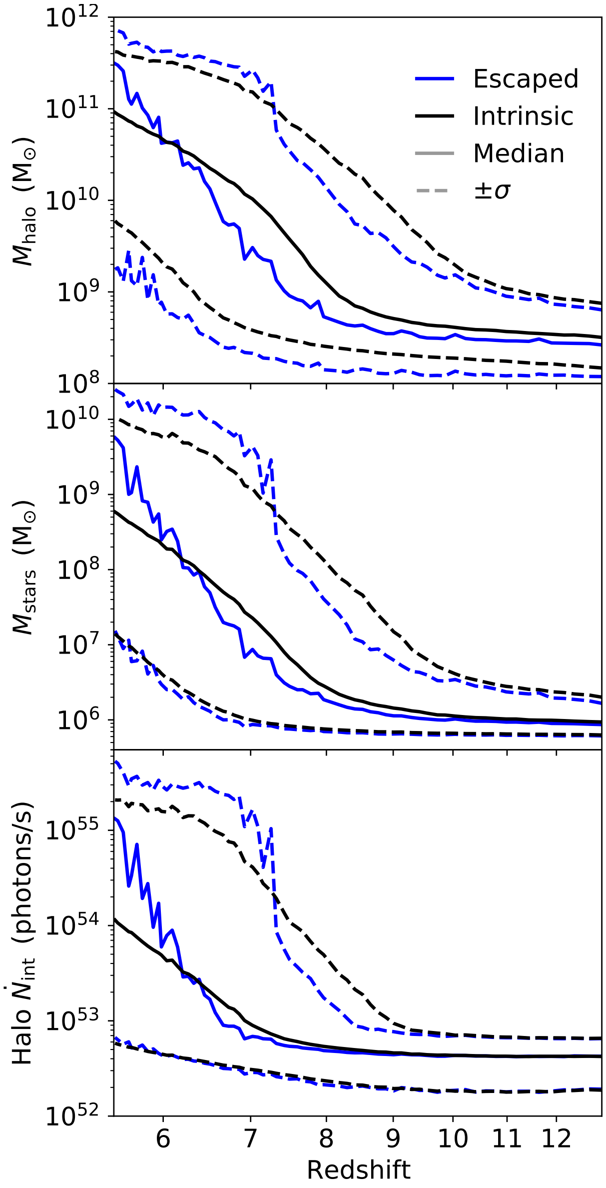

Figure 3-4: Halo masses, stellar masses, and halo intrinsic photon rates (top, middle, and bottom panels, respectively) that contribute to $\{16, 50, 84\}\,\%$ of the global escaped and intrinsic photons (blue and black curves, respectively) when sorted by these quantities across redshifts $z = 5.5$–13. The increasing median $M_{\rm halo}$, $M_{\rm stars}$, and $\dot{N}_{\rm int}$ as redshift decreases clearly illustrates the growing importance of massive and bright haloes towards lower redshifts.

massive galaxies in Fig. 3-4, where we plot the corresponding M_{halo} (top panel), M_{stars} (middle panel), and halo $\dot{N}_{\mathrm{int}}$ (bottom panel) that contribute to $\{16, 50, 84\}\,\%$ of the global escaped (blue) and intrinsic (black) photons when sorted by these quantities, all as functions of redshift. The median M_{halo}, M_{stars}, and $\dot{N}_{\mathrm{int}}$ increase over time in terms of both global intrinsic and escaped photons. Moreover, a particularly sharp increase in the escaped distribution can be seen below $z \lesssim 7$, emphasizing the role of the brightest and most massive galaxies in accelerating reionization. Their importance mainly stems from their exceedingly high intrinsic photon rates in combination with moderately higher escape fractions ($f_{\mathrm{esc}} \sim 0.1$). Similarly, although there are larger numbers of faint galaxies with high f_{esc}, their combined impact on reionization is minor. These conclusions are consistent with the late-reionization model supported by recent observations and simulations (e.g. Naidu et al., 2020; Ma et al., 2020; Yung et al., 2020).

Chapter 4

Dependence on halo properties

4.1 Luminosity functions

We now investigate the key physical quantities that determine the escape fractions of individual haloes. The dependence on halo mass has been studied in previous cosmological simulations where the results suggest an anti-correlation between halo mass and escape fraction (Paardekooper et al., 2015; Kimm et al., 2017). However, these specific studies were limited to haloes with $M_{\text{halo}} \lesssim 10^9 \text{M}_{\odot}$ due to the high computational cost associated with simulating larger volumes at comparable resolutions. Here we take advantage of the significantly improved statistics provided by the THESAN simulation to explore the halo mass dependence of f_{esc} extended to higher mass galaxies. Specifically, we examine trends for individual haloes covering a mass range of $M_{\text{halo}} \in 10^8$–$10^{12}\,\text{M}_{\odot}$. Haloes with masses below this range are generally not resolved in the simulation. On the other hand, haloes with masses above this range are not found in the THESAN simulation due to the limited volume of the simulation.

To characterize the halo source population, in the top panel of Fig. 4-1 we show cumulative luminosity functions for the intrinsic (dashed) and escaped (solid) photon rates $\dot{N}$ for all haloes in the same redshift bin ranges as before covering $z = 5.5$–13. There is a clear evolution with redshift due to the increase of bright haloes as they start to dominate the total photon rate density. The rightmost ends of the curves show the largest photon rate from a single halo at a given redshift, which also

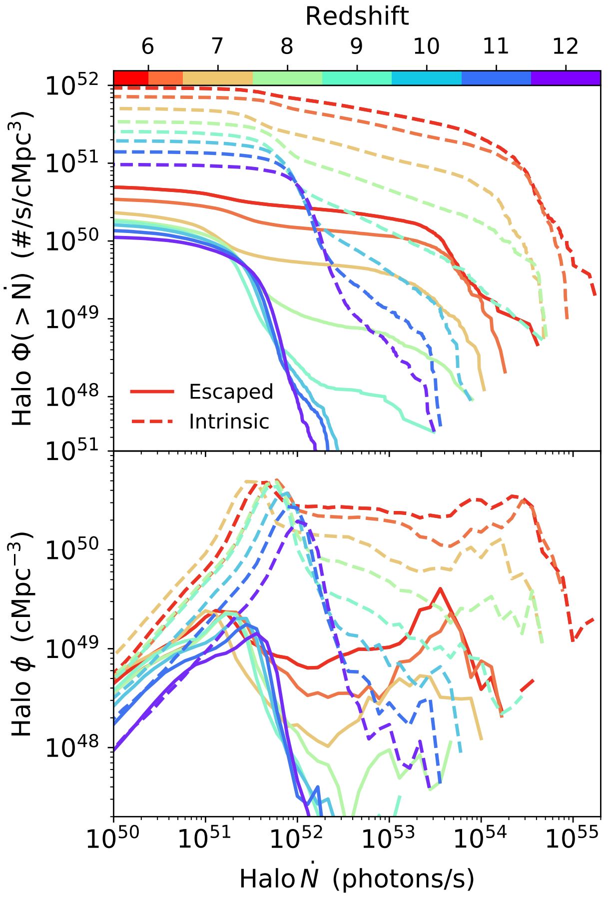

Figure 4-1: *Top:* Cumulative luminosity functions for the intrinsic (dashed) and escaped (solid) photon rates $\dot{N}$ for all haloes in redshift bins covering redshifts from $z = 5.5$–13 as ranges indicated in the colour bar. There is a clear evolution revealing an increase of bright haloes starting to dominate the total photon rate density as redshift decreases. The rightmost points show the largest halo photon rate in the redshift bin, which also increases with the formation of more massive haloes. The curves flatten off when the cumulative contribution of fainter haloes is no longer significant. *Bottom:* Luminosity functions for both intrinsic and escaped halo photon rates. The number of haloes increases as the halo photon rate decreases at all redshifts. Brighter haloes are increasingly present at lower redshifts due to galaxy formation.

increases with time as more massive haloes form. The curves become increasingly flat as fainter halo sources no longer contribute significantly compared to brighter ones. The bottom panel of Fig. 4-1 shows the distribution of halo source population, again with intrinsic (dashed) and escaped (solid) photon rates in the same redshift range $z = 5.5$–13.

4.2 Median escape fractions

To better connect the halo properties with these sources, in Fig. 4-2 we show the dependence of the median halo intrinsic (dashed) and escaped (solid) photon rate ($\dot{N}$; top) and escape fraction ($f_{\rm esc}$; bottom) on halo mass ($M_{\rm halo} \in 10^8$–$10^{12}\,{\rm M}_\odot$; left), stellar mass ($M_{\rm stars} \in 10^6$–$10^{10}\,{\rm M}_\odot$; middle), and star-formation rate (${\rm SFR} \in 10^{-3}$–$10^2\,{\rm M}_\odot\,{\rm yr}^{-1}$; right) for all selected haloes in different redshift ranges from $z = 5.5$–13. We emphasize that the median escape fractions behave differently than the global ones presented in Fig. 3-3, mostly because the medians and means statistics are very different in this case. In addition, the global averages include both bright outliers and stars outside the virial radius, and thus are not exactly the same as the $f_{\rm esc}$ we defined in Eqn. 2.1. The haloes at the low-mass end have escape fractions close to the birth cloud value of $f_{\rm esc}^{\rm cloud} = 0.37$, indicating that almost all photons reach the IGM once they escape the birth cloud. This maximal escape behaviour of low-mass haloes also justifies our assumption of adopting this value for non-selected haloes in Chapter 3. As the halo mass increases, the median $f_{\rm esc}$ drops significantly with a minimum around $M_{\rm halo} \sim 10^9\,{\rm M}_\odot$. The decrease of $f_{\rm esc}$ at the low mass end agrees with the results from the above-mentioned studies, but in our case this is clearly also driven by resolution limitations and a selection bias towards haloes with higher stellar-to-halo mass ratios, which might lead to an overestimation of $f_{\rm esc}$ at the low-mass end. The median $f_{\rm esc}$ remains low with $f_{\rm esc} \sim 0.01$ at $z \sim 6$ in intermediate mass haloes with an observed gradual increase in $f_{\rm esc}$ as halo mass increases up to about $M_{\rm halo} \sim 10^{11}\,{\rm M}_\odot$ at all redshifts. Finally, $f_{\rm esc}$ has a steep increase for haloes above this mass, as can be seen at lower redshifts. This may result from ionizing channels created by other mechanisms,

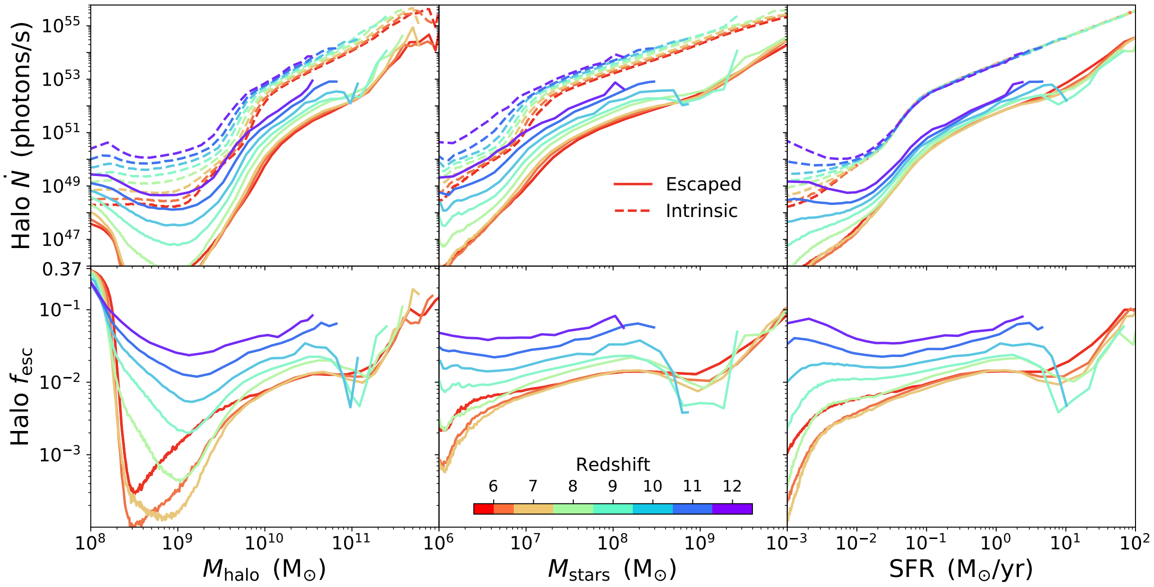

Figure 4-2: *Top:* The median values of the intrinsic (dashed) and escaped (solid) photon rates as a function of halo mass (left), stellar mass (middle), and SFR (right) for all selected haloes across several redshift ranges covering $z = 5.5$–13 as indicated in the colour bar. Haloes falling within the same redshift ranges are combined. The binning is adapted based on the halo number distribution with more bins towards the high-mass end to account for the fewer amount of haloes available in these ranges. The figure includes all the selected galaxies with criteria defined in 2.2, ranging from 10^8–$10^{12}\,\mathrm{M}_\odot$. The intrinsic photon rate increases as halo mass increases, and the flattening at the low-mass end is again due to the baryonic mass resolution of the THESAN simulation. The escaped photon rate drops to the minimal at $M_{\rm halo} \approx 10^9\,\mathrm{M}_\odot$ and increases beyond this point. *Bottom:* The median of $f_{\rm esc}$ as a function of $M_{\rm halo}$ with the same binning method and halo selection criteria as above. The escape fractions reach the maximal value of 0.37 for lowest-mass haloes, and decrease as a function of halo mass afterwards. $f_{\rm esc}$ reach the minimal values at $M_{\rm halo} \approx 10^9\,\mathrm{M}_\odot$. For haloes more massive than this value, the $f_{\rm esc}$ gradually increases as halo mass increases. Some very massive haloes at low redshifts ($M_{\rm halo} > 10^{11}\,\mathrm{M}_\odot$) can reach $f_{\rm esc} = 0.1$. A clear redshift dependence can be seen from the figure with higher $f_{\rm esc}$ at higher redshifts.

e.g. powerful feedback associated with massive galaxies. We will discuss the impact of dust at the high mass end in Chapter 6.1. Comparing the curves in different redshifts, we see $f_{\rm esc}$ increases with redshift in all mass ranges. Similar trends are also reported in several previous studies (Eide et al., 2020; Faucher-Giguère, 2020; Ma et al., 2020).

Furthermore, since $f_{\rm esc}$ is defined to be the ratio of the escaped and intrinsic photon rates, it is interesting to also examine the change in both quantities as a function of halo mass. At all redshifts, the medians of intrinsic and escaped photon rates increase with the halo mass, stellar mass, or star-formation rate, although the curves become relatively flat at the low-mass end (Fig. 4-2). The MCRT procedure requires at least one star within the virial radius as a photon source in the calculation, and therefore the intrinsic photon rates do not further decrease as halo mass decreases at the low-mass end due to the limited mass resolution in the simulation. The escaped photon rates reach the lowest point at $\approx 10^9\,{\rm M}_\odot$, and reach the highest point at the high-mass end. In all redshifts, we notice higher photon rates at higher redshifts for a given halo mass range. This can be attributed to changes in the stellar population as galaxies assemble and evolve. In fact, the specific star formation rate in the halo decreases with time (see Figure 1 of Kannan et al., 2021), which explains why this evolution is not apparent in the rightmost panel of Fig. 4-2 showing the intrinsic photon rate as a function of the SFR.

The non-monotonic dependence of $f_{\rm esc}$ on the halo mass strongly suggests that there are additional factors that can affect the escape of ionizing photons. In particular, the stellar mass and star-formation rate are two of the more intuitive quantities since star-forming galaxies are believed to play a crucial role in reionization and many reported measurements of $f_{\rm esc}$ come from starburst galaxies. Overall, the median curves in Fig. 4-2 reveal a flatter or more moderate dependence on $M_{\rm stars}$ and SFR, except at the highest ranges, while the redshift evolution is strong before the midpoint of reionization.

4.3 Effective SFR surface density

Beyond the cumulative and instantaneous star formation history, we expect the relative amount and density of absorbing hydrogen atoms in the surrounding gas reservoir to affect halo escape fractions. We therefore explore several of these features in Fig. 4-3. In the top panel we show the distribution of $f_{\rm esc}$ in a 2D plane of SFR and $M_{\rm halo}$ for galaxies at redshifts of $z = \{10, 8.5, 7, 5.5\}$. The median and 1σ variation ($16^{\rm th}$ and $84^{\rm th}$ percentiles) of $f_{\rm esc}$ at each mass bin is shown in the black solid and dashed curves, respectively. It is clear that the SFR increases as the halo mass increases in all mass ranges as expected. Galaxies with the highest $f_{\rm esc}$ have a combination of lower mass and higher SFR as highlighted in the yellow regions. For slightly more massive haloes ($M_{\rm halo} > 10^{10}\,{\rm M}_{\odot}$), $f_{\rm esc} < 10\%$ even with high SFRs. In the low-mass region, the distribution of SFR at a given halo mass is wider and thus allows some haloes to have high $f_{\rm esc}$. On the other hand, the distribution of SFR in high-mass regions is relatively narrow and a typical massive halo does not have sufficient SFR to produce high $f_{\rm esc}$ in our simulation.

In the middle panel of Fig. 4-3, we show the SFR surface density $\Sigma_{\rm SFR} \equiv {\rm SFR}_{r_e}/(2\pi r_e^2)$, with r_e denoting the half stellar mass radius as this is observationally accessible (although see Trujillo et al., 2020), and ${\rm SFR}_{r_e}$ to be the SFR within the half stellar mass radius. This is additionally motivated by the fact that many of the LyC leakers have higher than average $\Sigma_{\rm SFR}$ (Naidu et al., 2020). Recent observational efforts have also been focused on the dependence of $f_{\rm esc}$ on $\Sigma_{\rm SFR}$. In particular, it was pointed out that a large sample is required to identify the relation between $f_{\rm esc}$ and $\Sigma_{\rm SFR}$ (Pahl et al., 2022). Our figure shows that at a given halo mass, galaxies with higher $\Sigma_{\rm SFR}$ have higher $f_{\rm esc}$, but it does not solely determine $f_{\rm esc}$ either as there is a significant degree of mixing between higher and lower $f_{\rm esc}$ values.

In an attempt to find a discriminating quantity that correlates with $f_{\rm esc}$ in a monotonic manner, we modify the concept of $\Sigma_{\rm SFR}$ by dividing SFR by the gas mass $M_{\rm gas}$ and replacing a stellar-based radius with the virial radius R_{200}. We denote this new heuristic but theoretically motivated quantity as $\overline{\Sigma}_{\rm SFR} = {\rm SFR}/M_{\rm gas}/R_{200}^2$. This

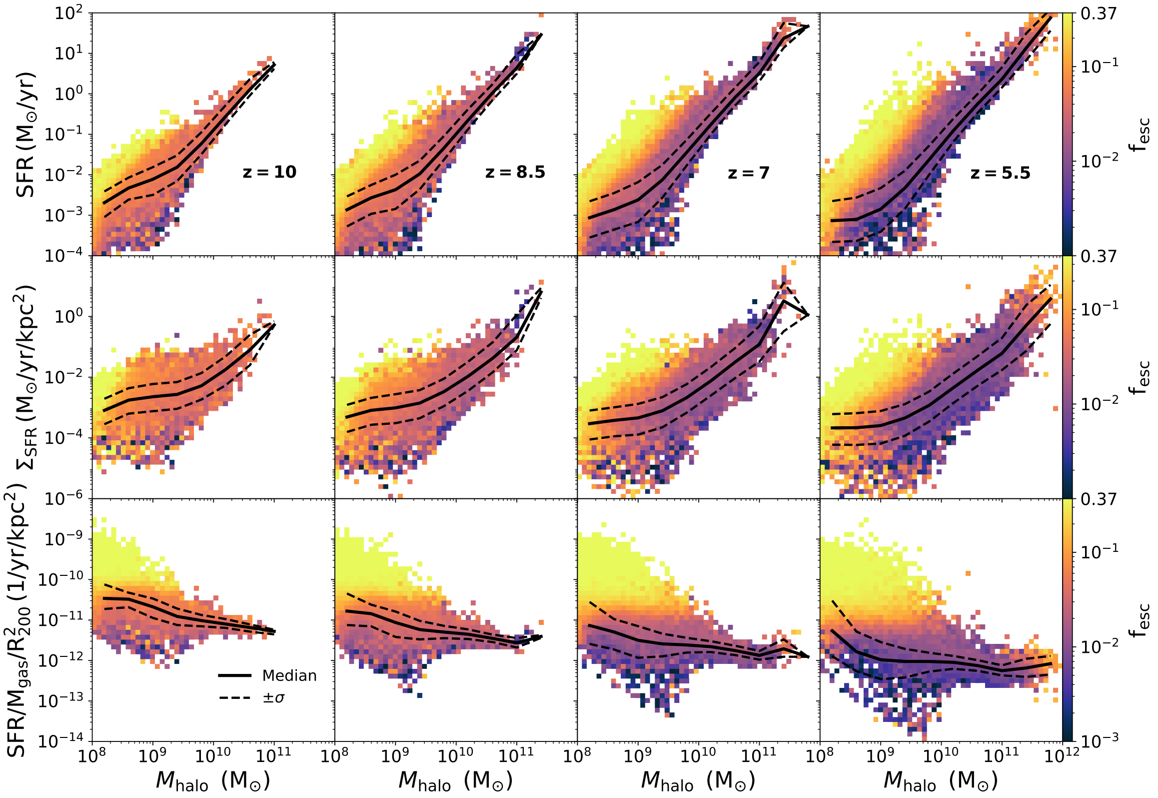

Figure 4-3: Distribution of haloes at $z = \{10, 8.5, 7, 5.5\}$, from left to right, with various masses and star formation rates (SFR, top), surface SFR ($\Sigma_{\rm SFR}$ as defined in Pahl et al. (2022) with r_e = half stellar mass radius, middle), and modified surface SFR per gass mass ($\overline{\Sigma}_{\rm SFR} = {\rm SFR}/M_{\rm gas}/R^2_{200}$, bottom). The 2D histograms are coloured by $f_{\rm esc}$ with 50 bins in both axes, and each bin is normalized by the number of haloes as in Fig. 2-1. The median values are show in the black solid curves and the 16th and 84th percentiles are shown in the black dashed curve. At each redshift, haloes with relatively low masses and high SFRs have the highest escape fractions. For massive haloes ($M_{\rm halo} > 10^{10}\,{\rm M}_{\odot}$), $f_{\rm esc} < 10\%$ even with high SFRs. In addition, in the low-mass haloes, the distribution of SFRs is wider and thus allows haloes with higher than usual SFR to have high $f_{\rm esc}$. On the other hand, the distribution of SFR in high-mass regions is relatively narrow and a typical massive halo does not have sufficient SFR to produce high $f_{\rm esc}$ in our simulation. In the middle panel, $\Sigma_{\rm SFR}$ shows a similar trend as SFR. In the bottom panel, the histograms are seen to be divided into two regions by $\overline{\Sigma}_{\rm SFR}$, suggesting that this quantity is a potential discriminator for $f_{\rm esc}$.

particular combination is chosen since the gas mass of a galaxy roughly correlates with the amount of neutral hydrogen needed to be ionized before LyC photons can escape to the IGM. The bottom panel in Fig. 4-3 shows the distribution of f_{esc} with respect to $\overline{\Sigma}_{\mathrm{SFR}}$ and the halo mass. The median values $\overline{\Sigma}_{\mathrm{SFR}}$ drop slightly as halo mass increase from 10^8 to $10^9\,\mathrm{M}_{\odot}$, but do not change significantly as the halo mass increases further. Moreover, there is a strong colour gradient in the vertical direction and relatively little variation along the horizontal direction indicating that $\overline{\Sigma}_{\mathrm{SFR}}$ correlates with f_{esc} in a simpler way than using M_{halo} or SFR alone. However, we note that the escape of ionizing photons is a complex process, and the construction of $\overline{\Sigma}_{\mathrm{SFR}}$ does not include other potentially important mechanisms such as AGN feedback in massive haloes.

Chapter 5

Variations in the escape fractions

In the previous chapter, we discussed relationships between various physical quantities and the *median* escape fraction. While this provides an intuitive picture for the sources of reionization, it does not fully represent the rich statistics across the entire ensemble of galaxies. In particular, bright outliers with $\dot{N}_{\rm esc}$ above the median can play more important roles in the reionization process. In this chapter, we further discuss the distribution of $f_{\rm esc}$ and photon rates.

5.1 Halo-to-halo variations

In Fig. 5-1 we show the normalized distribution of halo escape fractions $f_{\rm esc}$ (top panels) along with intrinsic and escaped photon rates $\dot{N}$ (bottom panels) as functions of halo mass $M_{\rm halo}$ at the specific redshifts $z = \{10, 8.5, 7, 5.5\}$. The figure includes all selected haloes from the individual snapshots and each vertical histogram is normalized by the number of haloes in the given mass bin. The red solid lines in the top panels show the median halo $f_{\rm esc}$ in each mass bin, and the dashed lines indicate the $16^{\rm th}$ and $84^{\rm th}$ percentiles. Likewise, the black (blue) solid lines show the medians of the intrinsic (escaped) photon rates, and the associated dashed lines correspond to the $16^{\rm th}$ and $84^{\rm th}$ percentiles. At low halo mass, $f_{\rm esc}$ exhibits a wide distribution from 0.1–37% with the medians between 1–10% at $z = 10$ but extending down to 0.1% at later redshifts. This is consistent with the picture in Fig. 4-3 where $f_{\rm esc}$ can vary for

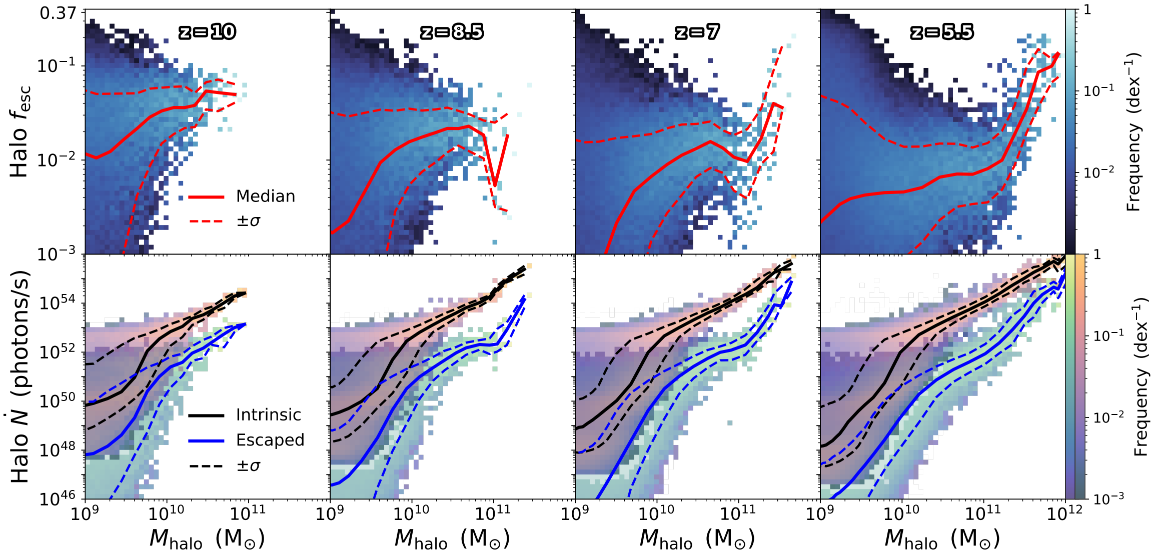

Figure 5-1: *Top:* Distribution of halo escape fractions $f_{\rm esc}$ as a function of halo mass $M_{\rm halo}$ at redshifts of $z = \{10, 8.5, 7, 5.5\}$, from left to right. Data below $10^9\,{\rm M}_\odot$ are not shown due to the lower completeness. The distribution is normalized by the number of haloes in each mass bin similarly to Fig. 2-1. The red solid curves show the median $f_{\rm esc}$ at a given mass bin, and the red dashed curves indicate the 16th and 84th percentiles. $f_{\rm esc}$ starts with a wide distribution at the low-mass end and becomes narrower for more massive haloes ($M_{\rm halo} \gtrsim 10^{10}\,{\rm M}_\odot$). At the massive end ($M_{\rm halo} \gtrsim 10^{11}\,{\rm M}_\odot$), almost all haloes have $f_{\rm esc} \sim 10\%$ although they only occur at $z \lesssim 7$. *Bottom:* The distributions of intrinsic and escaped photon rates $\dot{N}$ as functions of halo mass. In both cases, the scatter is large at the low-mass end and becomes smaller above $M_{\rm halo} \gtrsim 10^{10}\,{\rm M}_\odot$, with the escaped photon rate distributions being wider than the intrinsic ones.

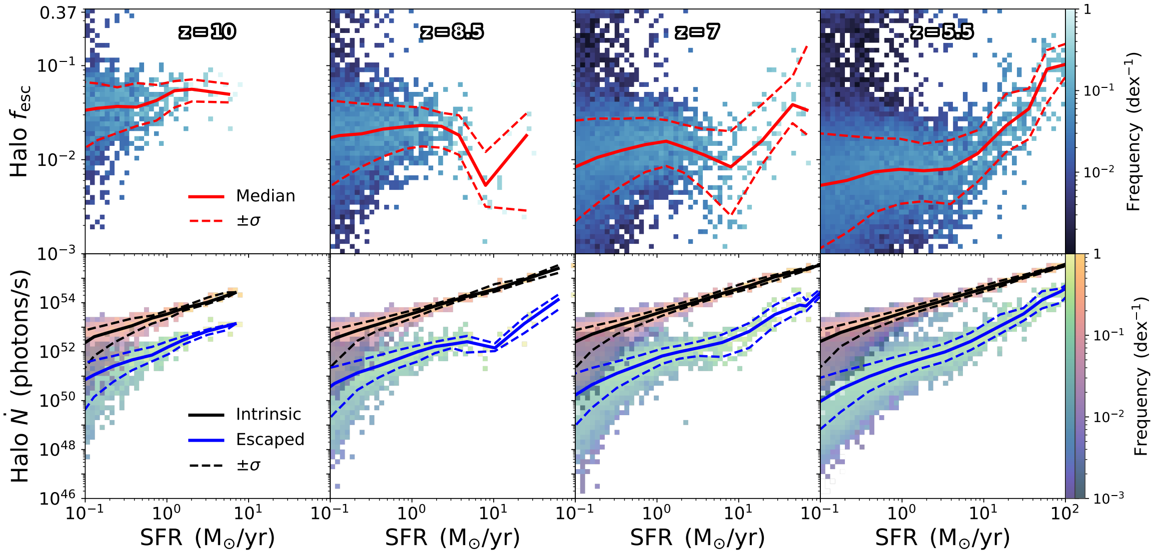

Figure 5-2: *Top:* Distribution of halo escape fractions $f_{\rm esc}$ as a function of the star-formation rate at redshifts of $z = \{10, 8.5, 7, 5.5\}$, from left to right. All plotting styles and data representations are identical to Fig. 5-1, specifically the solid and dashed coloured curves indicate the median and 1σ percentiles. As before, $f_{\rm esc}$ have a large scatter at the low-SFR end and a narrower distribution as the SFR increases. *Bottom:* The distributions of intrinsic and escaped photon rates $\dot{N}$ as functions of the SFR. Intrinsic photon rates correlate extremely well with SFR, such that the variation in escape fractions drives the IGM source distribution at a given SFR.

galaxies with similar masses because of different SFRs in different galaxies. In addition, a significant amount of medium-sized galaxies with masses below $\lesssim 10^{10}\,\mathrm{M}_\odot$ have $f_\mathrm{esc} \lesssim 10^{-3}$ at $z = 7$. As M_halo further increases, the distribution becomes narrower and most haloes have percent level escape fractions. The largest haloes with $M_\mathrm{halo} \gtrsim 10^{11}\,\mathrm{M}_\odot$ generally have a higher f_esc, but are not commonly found in our simulated volume above redshift $z = 8.5$.

In Fig. 5-2 we show the same distributions for f_esc and $\dot{N}$ as functions of SFR ranging from 0.1–100 $\mathrm{M}_\odot$/yr at redshifts $z = \{10, 8.5, 7, 5.5\}$. Haloes with SFRs higher than $100\,\mathrm{M}_\odot$/yr are rarely seen in the simulation, and the region below $0.1\,\mathrm{M}_\odot$/yr is clipped due to the lower resolution below this range. In comparison to Fig. 5-1, SFRs better characterize the intrinsic photon rates of a halo as the distributions are generally narrower for SFRs than M_halo. At all redshifts, the variation in the intrinsic photon rates as a function of SFR is relatively small compared to that of halo mass, especially for haloes with SFRs higher than $1\,\mathrm{M}_\odot$/yr. The intrinsic distributions widen for galaxies with lower SFRs. The distributions for the escaped photon rates remain quite complex due to the combined scatter from intrinsic photon production and escape fraction physics. Overall, we conclude that the strong sensitivity of f_esc to ISM and CGM scale processes is the main factor in setting the variation in escaped sources into the IGM throughout the EoR.

5.2 Sightline statistics

In the previous chapters, we have presented results from the angular-averaged f_esc from all stellar sources escaping the surface of a sphere at R_{200}. However, it should not be surprising that the escape fractions also have a large sightline-to-sightline variability due to the anisotropic distribution of the matter within galaxies. In this section, we aim to capture the anisotropic structure using the ray-tracing techniques implemented in COLT to calculate f_esc for observers oriented along each of $N = 3072$ healpix directions of equal solid angle.

Analyzing the data from sightline statistics allows for deeper understandings into the underlying escape fraction physics. For example, we can answer the following questions: What is the variability of $f_{\rm esc}$ from different sightlines? Do most of the photons escape through a handful of ionizing channels consistent with the concept of a covering fraction, or is a more isotropic picture favoured? What is the percentage of sightlines with $f_{\rm esc}$ higher than the mean escape fraction? How do these answers also depend on halo properties?

To understand the anisotropic features of sightline dependent escape fractions in a more quantitative way, we define the following five quantities for each selected halo: (1) normalized covering fraction $P(f_{\rm esc} > \langle f_{\rm esc} \rangle)$ as the fraction of sightlines that have escape fractions higher than the mean escape fraction $\langle f_{\rm esc} \rangle \equiv \frac{1}{N}\Sigma_{i=1}^{N} f_{\rm esc,i}$, (2) standard deviation of the sightline escape fractions $\sigma_{\rm esc}^2 \equiv \frac{1}{N}\Sigma_{i=1}^{N}(f_{\rm esc,i} - \langle f_{\rm esc} \rangle)^2$, (3) normalized standard deviation of the sightline escape fractions as $\sigma_{\rm esc}/\langle f_{\rm esc} \rangle$, (4) half flux area, which is defined as the fractional area of the sphere contributing half of the escaped photons when sorted from brightest to faintest, and (5) the Gini coefficient G measuring the statistical dispersion in terms of equity of sightline distributions. Specifically, the Gini coefficient

$$G = \frac{2\Sigma_{i=1}^{N} i f_{\rm esc,i}}{N\Sigma_{i=1}^{N} f_{\rm esc,i}} - \frac{N+1}{N} \,, \tag{5.1}$$

always lies in the range $[0, 1]$ with values near unity representing significant anisotropy (escape dominated by a few sightlines) and small values representing significant isotropy (all sightlines contributing equally). As we will also make our escape fraction catalogues publicly available we defer more specialized viewing dependence analyses to future studies.

In Fig. 5-3 we present the distributions of these five quantities as functions of halo mass at redshifts of $z = \{10, 8.5, 7, 5.5\}$. The median and 1σ deviation (16th and 84th percentiles) are also shown in black solid and dashed lines, respectively. In the top panel, P represents the fraction of sightlines with higher-than-average escape fractions for each selected halo. At all redshifts, these normalized covering fractions have a wide distribution for less massive haloes $M_{\rm halo} \lesssim 10^{10}\,{\rm M}_{\odot}$, ranging from 0.01

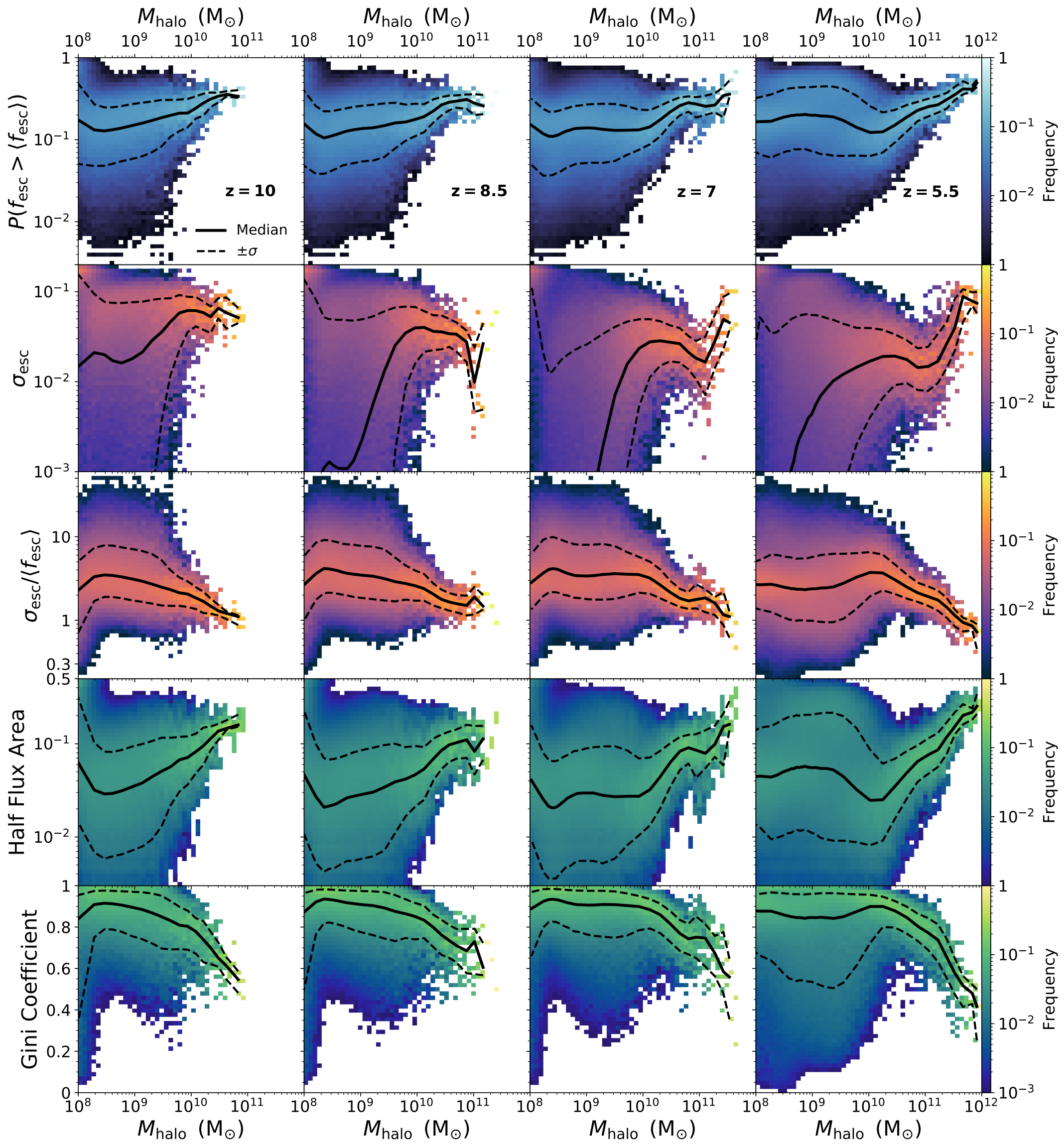

Figure 5-3: Distribution of covering fractions relative to the mean $P(f_{\rm esc} > \langle f_{\rm esc}\rangle)$ (top), standard deviations of escape fractions $\sigma_{\rm esc}$ (second), and normalized standard deviations $\sigma_{\rm esc}/f_{\rm esc}$ (third), half flux area (fourth), and the Gini coefficient G (bottom; defined in Eqn. 5.1) of all selected haloes as a function of $M_{\rm halo}$ at redshifts of $z = \{10, 8.5, 7, 5.5\}$. The median and 16th and 84th percentiles are also shown in black solid and dashed lines, respectively. Most haloes have covering fractions P falling between 0.05 and 0.4, i.e. a minority of sightlines influences the mean. There is no significant dependence on redshift but a qualitative increase for the highest mass haloes. The third panel shows that the standard deviations of sightline escape fractions in most haloes are above $\langle f_{\rm esc}\rangle$, and the median of the normalized standard deviation decreases as halo mass and mean escape fraction increase. The fourth panel shows an increasing half flux area as halo mass increases, emphasizing the importance of sightlines that are not among the highest ones. The Gini coefficient in the bottom panel similarly shows a more isotropic and equitably distributed picture at the high-mass end.

to almost 1 with 68% of haloes having $P \in [0.05, 0.4]$. The black solid curves suggest that in the median case, only 10–20% of sightlines have $f_{\rm esc}$ higher than their mean at all redshifts, revealing a substantial degree of anisotropy as $\langle f_{\rm esc} \rangle$ is influenced by a small minority of sightlines. On the other hand, the distribution of P is much narrower among high mass haloes. For example, most of the haloes with $M_{\rm halo} > 10^{11}\,{\rm M}_\odot$ have normalized covering fractions increasing to 30–50% by $z = 5.5$. This indicates that the sightline variability is more drastically different from halo to halo in low-mass haloes than in high-mass ones.

In the second and third panels, the standard deviation and normalized standard deviation provide a direct intuitive measure of the variability among sightlines. In particular, $\sigma_{\rm esc}/\langle f_{\rm esc} \rangle$ evaluate the standard deviations in the unit of the angle-averaged escape fractions. The third panel shows that at all redshifts the majority of haloes have sightline standard deviations larger than $\langle f_{\rm esc} \rangle$. Similar to the distribution of the covering fractions P, standard deviations also have a wider distribution among lower-mass haloes while transitioning to a smaller scatter for the highest-mass haloes. Given these trends of increasing standard deviation and decreasing normalized standard deviation with halo mass, we interpret this as a transition from a low-escape high-anisotropic mode at $M_{\rm halo} \lesssim 10^{10}\,{\rm M}_\odot$ to a more structured, large opening angle, and steady mode of escape at the highest masses.

The second to last panel in Fig. 5-3 shows the half flux area as defined above. The area gradually increases with halo mass, showing a notable increase above $M_{\rm halo} \gtrsim 10^{10}\,{\rm M}_\odot$ at $z \lesssim 7$. The low median values for low-mass haloes indicate that the halo $f_{\rm esc}$ are largely dominated by few sightlines with high escape fractions. In particular, half of the escaped photons are decided by the highest 1–10% of sightlines for low mass haloes, but the number rises to $\approx 25\%$ with less variation for the most massive haloes. This shows that the escape is not limited to a few high-$f_{\rm esc}$ sightlines, and more ionizing channels are present in massive haloes. This picture provides a potential explanation of the increase in halo $f_{\rm esc}$ with $M_{\rm halo}$ as shown in Fig. 4-2. The more extreme intrinsic luminosities and structured environments of massive haloes foster the creation of either more ionized channels or a few dominant ones with larger opening angles, and thus leads to overall higher escape fractions.

Finally, the Gini coefficient G in the bottom panel compares the contribution from high-$f_{\rm esc}$ and low-$f_{\rm esc}$ sightlines. At all redshifts, most low-mass haloes have G close to unity, meaning the sightline distributions are highly skewed. G deviates from unity as halo mass increases, and reaches $G \approx 0.5$ for the most massive haloes at $z = 5.5$. This shows a more equally distributed contribution from all sightlines. Therefore, the measure from the Gini coefficient G is consistent with the result from the half flux area.

5.3 Angular structure correlations

The anisotropic behaviour has also been discussed in other studies (Paardekooper et al., 2015; Trebitsch et al., 2017), showing that most of the ionizing photons escape from galaxies through low column density channels. In Fig. 5-4 we provide visualizations of the angular distribution of the escape fraction $f_{\rm esc}$, hydrogen absorption $f_{\rm HI}$, helium absorption $f_{\rm HeI} + f_{\rm HeII}$, hydrogen column density $N_{\rm H}$ (normalized by the mean), and mean absorption distance $\langle \ell \rangle$ (normalized by the virial radius) in the most massive haloes at redshifts of $z = \{10, 8.5, 7, 5.5\}$, respectively. Below each image, we show the mean (left) and median $\pm 1\sigma$ (right) statistics based on 3072 healpix directions, with the exception of the hydrogen column density and absorption distance where for convenience we report the halo-dependent mean logarithmic column density (in log cm^{-2}) and virial radius (in kpc) at the left. The absorption from hydrogen and helium is calculated using Eqn. (2.2), with $f_{\rm He}$ representing the combined absorption of HeI and HeII. The dust density has been set to zero and thus $f_{\rm abs} = 0$ in this calculation. In general, by construction the sum of $f_{\rm esc}$ and the absorption from different species equals the birth cloud escape fraction as can be calculated from the following equation: $f_{\rm esc}^{\rm cloud} = f_{\rm esc} + f_{\rm HI} + f_{\rm He} + f_{\rm abs}$.

In greater detail, to more fairly compare the four different haloes, the hydrogen column density has been normalized by the angular-averaged value for each halo. Each sightline is the intrinsic photon rate weighted value from each star, i.e.

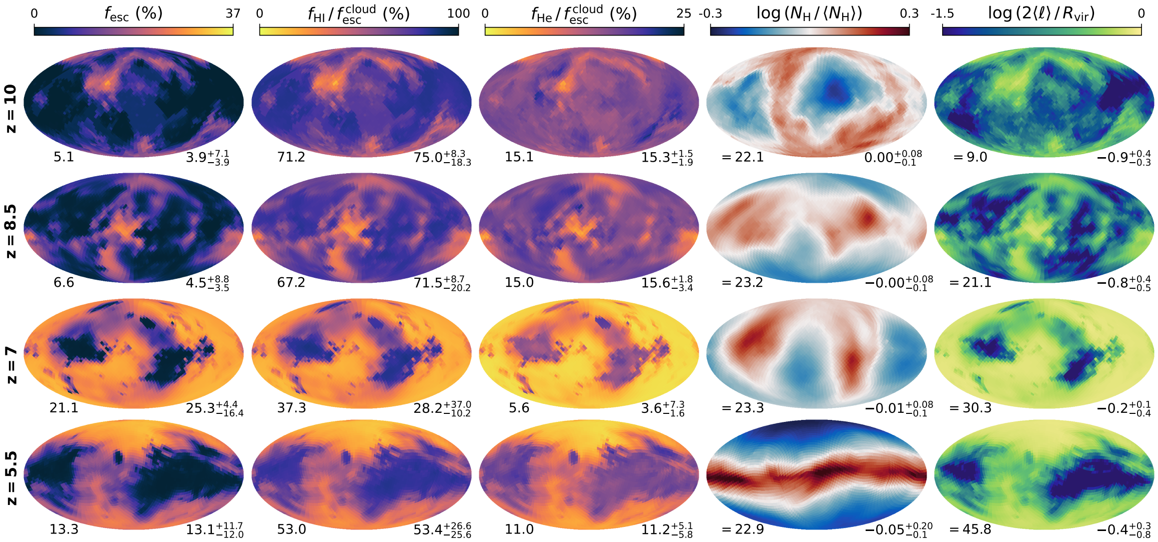

Figure 5-4: Healpix plots of various physical quantities in the most massive galaxies at redshifts of $z = \{10, 8.5, 7, 5.5\}$, respectively. From left to right these are: LyC escape fraction f_{esc}, hydrogen absorption fraction f_{HI} (normalized by $f_{\mathrm{esc}}^{\mathrm{cloud}}$), helium absorption fraction $f_{\mathrm{HeI}} + f_{\mathrm{HeII}}$ (also normalized), hydrogen column density N_{H} (normalized by the mean hydrogen column density of 3072 directions), and mean absorption distance $\langle \ell \rangle$. The dust density has been set to zero in this calculation. In the lower left (right) of each map we provide the average (median and 1σ variation) of all 3072 sightlines, with the exception of the column density and absorption distance where for convenience we report the halo-dependent mean logarithmic column density (in cm^{-2}) and virial radius (in kpc), respectively. Formulae used in the calculation of absorption and mean absorption distance are discussed in Sec. 2.

$N_{\mathrm{H}} \equiv \sum \dot{N}_{\mathrm{int},i} N_{\mathrm{H,i}} / \sum \dot{N}_{\mathrm{int},i}$. Similarly, the mean absorption distance is normalized by the virial radius of the halo. The mean absorption distance corresponds to the typical distance photons travel before being absorbed, as defined in Eqn. 2.3. Note that the maximum mean optically thin absorption distance equals half the virial radius as can be seen by setting $k_a = 0$ in Eqn. 2.3. Our results clearly demonstrate the anisotropic behaviour of f_{esc}. Moreover, the morphologies of the direct radiative transfer quantities (i.e. with some exceptions for N_{H}) are strikingly similar, indicating correlations among them at the sightline level. In particular, f_{esc} strongly correlates with the mean absorption distance but anti-correlates with the hydrogen and helium absorption fractions. In other words, the photons can travel longer distances and escape the halo along low column density sightlines, resulting in lower f_{HI}, f_{He} and thus higher f_{esc}. Finally, disk-like structures from the forming galaxy manifest themselves in the bipolar distribution of the sightline statistics, with higher f_{esc} in the direction perpendicular to the plane of the disk. The high anisotropy found in the values of f_{esc} from various sightlines also implies the measured f_{esc} can be highly dependent on the direction being measured (edge-on or face-on). It therefore presents a potential challenge for comparing simulations to observations, which are more or less randomly oriented. Of course, lower-mass galaxies will have different morphologies and characterizing the anisotropic sourcing of LyC radiation during the EoR is worth a more detailed investigation, especially if small-to-large scale (ISM, CGM, and IGM) connections cascade to affect the bubble topology of reionization.

Chapter 6

Model uncertainties

We now discuss the main caveats of our analysis and when possible quantify the level of uncertainties, starting with dust absorption, AGN emission, and galaxy formation modelling. A discussion of resolution and convergence is presented in Appendix A.

6.1 Dust absorption

As briefly noted in Chapter 2, THESAN does not include on-the-fly dust absorption for ionizing photons, mostly because dust modelling in the high-redshift Universe remains relatively unconstrained. Including dust would mainly translate to a slightly different behaviour for the radiation field in high mass galaxies. While it is worth exploring the impact of on-the-fly dust absorption in THESAN, also in the context of sub-resolution ISM and feedback models, for consistency with the simulated ionization states we also do not include dust in our fiducial MCRT calculations. In this section, we focus on estimating the impact of dust on post-processed MCRT escape fractions.

Although THESAN incorporates the creation and destruction of dust, many physical processes relevant to dust occur at sub-parsec scales and thus the precise amount of dust in each cell might not be accurately determined. Thus, in addition to using the dust abundance modeled from the simulation, we also insert dust into the post-processing MCRT calculation using the redshift-dependent dust-to-metal ratio suggested by Vogelsberger et al. (2020b) (model C), which has been calibrated to

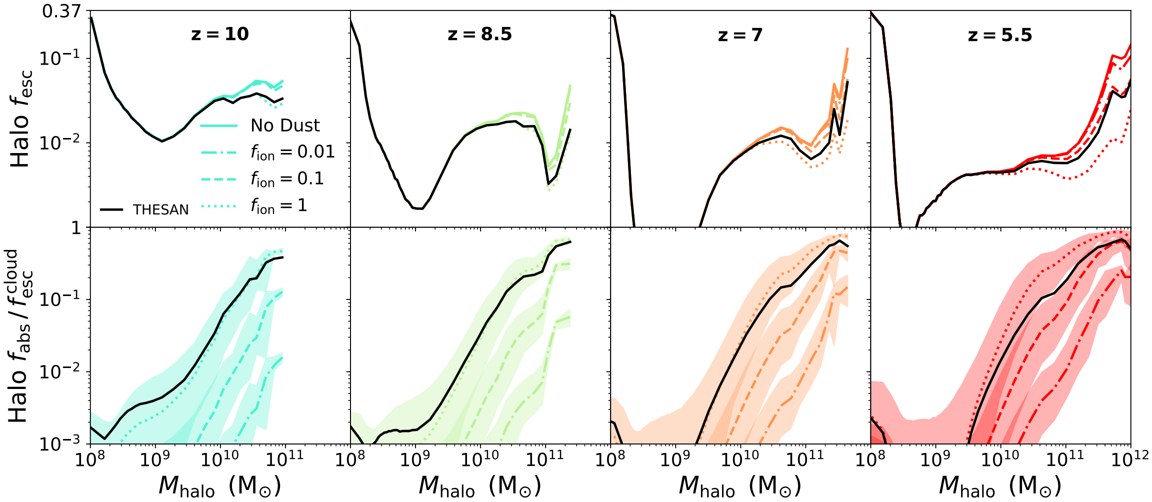

Figure 6-1: *Top:* Median values of halo escape fraction $f_{\rm esc}$ as a function of $M_{\rm halo}$ at $z = \{10, 8.5, 7, 5.5\}$ for five different dust scenarios: no-dust (fiducial; solid), redshift-dependent dust-to-metal ratio from Vogelsberger et al. (2020b) together with three different dust survival fractions in HII regions $f_{\rm ion} = \{0.01, 0.1, 1\}$ (dash-dot, dashed, dotted), and on-the-fly dust modelling from THESAN (black solid). The inserted dust in all cases does not affect the overall dependence of $f_{\rm esc}$ on the halo mass except at the high-mass end where a lower $f_{\rm esc}$ results from the higher dust content. The on-the-fly simulated dust model lies between $f_{\rm ion} = 0.1$–1. *Bottom:* Median values of $f_{\rm abs}$ as a function of halo mass shown for the same redshifts and same five dust scenarios as above. The shaded regions indicate the 16th and 84th percentiles across different haloes. $f_{\rm abs}$ is calculated by Eqn. (2.2) and increases as dust mass increases as expected.

match observed UV luminosity functions. In the latter case, we also adopt three different dust survival fractions in the HII regions of $f_{\rm ion} = \{0.01, 0.1, 1\}$ to empirically explore scenarios with varying degrees of reduced dust abundances in ionized regions. This is a common parametrization used within the Lyman-alpha radiative transfer community to increase escape fractions with the justification of being a proxy for generally harsh environments (Laursen et al., 2009). Specifically, the destruction processes correlate with local feedback and unresolved turbulence or shocks, as well as other mechanisms such as radiation pressure (Draine, 2011) or rotational disruption of dust grains by radiative torques in strong radiation fields (Hoang et al., 2019). We warn that values below $f_{\rm ion} \lesssim 0.1$ may not be realistic (see e.g. Hu et al., 2019; Kannan et al., 2020), however for our purposes the empirical model nonetheless provides a more continuous transition between the no dust and full dust scenarios. All the dust absorption opacities and anisotropic scattering are included based on the scattering albedo and Henyey–Greenstein phase function asymmetry parameter assuming the fiducial Milky Way dust model from Weingartner and Draine (2001).

In the top panel of Fig. 6-1 we show the median halo $f_{\rm esc}$ at redshifts of $z = \{10, 8.5, 7, 5.5\}$ in the presence of dust with the models described above. Results using the simulation-determined dust distributions and constant dust-to-metal scaling are shown as black and coloured curves, respectively. For reference, the coloured solid curves show the values from the fiducial no-dust scenario, while the various dashed and dotted line styles indicate partial or full survival in HII regions. The $f_{\rm esc}$ dependence on $M_{\rm halo}$ has a similar trend in all cases, with a noticeable difference at the high-mass end where $f_{\rm esc}$ decreases as $f_{\rm ion}$ increases. This is due to a higher amount of dust in high-mass haloes. In fact, the dust attenuation seems to compensate for the increased $f_{\rm esc}$ to flatten out the high-mass end. The impact of dust attenuation is also higher at the lowest redshift ($z = 5.5$) due to the production of metals and dust throughout the stellar evolution process along with the increased presence of massive galaxies. We note that the abundance of simulation-modeled dust lies between $f_{\rm ion} = 0.1$ and $f_{\rm ion} = 1$ at all redshifts examined. The bottom panel of Fig. 6-1 presents the median dust absorption $f_{\rm abs}$ as calculated by Eqn. 2.2 under the same

Global ionizing escape fraction f_{esc} [%]						
Redshift	No dust	$f_{\mathrm{ion}} = 0.01$	$f_{\mathrm{ion}} = 0.1$	$f_{\mathrm{ion}} = 1$	THESAN	$\frac{f_{\mathrm{ion}}=1}{\text{No dust}}$
13	14.2	14.2	14.2	14.1	14.2	99.3
11	10.6	10.6	10.6	10.5	10.5	99.1
10	10.8	10.8	10.8	10.7	10.7	99.1
9	7.67	7.67	7.66	7.58	7.58	98.8
8	6.05	6.03	5.96	5.78	5.82	95.5
7	5.61	5.42	5.03	4.55	4.82	81.1
6	5.95	5.53	4.55	3.58	4.23	60.2
5.5	5.18	4.51	3.25	2.25	3.05	43.4

Table 6.1: The impact on the global escape fraction assuming the same dust scenarios as in Fig. 6-1, including the fiducial no-dust case, redshift-dependent dust-to-metal ratio model with various empirical dust survival fractions of $f_{\mathrm{ion}} = \{0.01, 0.1, 1\}$, and the THESAN-modeled dust. Note that here we only present the instantaneous global escape fractions at $z = \{13, 11, 10, 9, 8, 7, 6, 5.5\}$, unlike in Fig. 3-2 where the values have been smoothed for presentation purposes. Including dust into the post-processing MCRT calculations has little influence at higher redshifts due to the relatively low dust abundances and halo masses at pre-reionization epochs. The impact increases as redshift decreases with a factor of ≈ 2 difference in the most extreme case by the end of the simulation.

five dust scenarios. The shaded regions illustrate the 1σ variation among the halo population. There is a clear increase in $f_{\rm abs}$ with halo mass, again due to a larger amount of dust present in massive haloes, but it is also interesting to see the order-of-magnitude offsets with $f_{\rm ion}$. The lowest redshift ($z = 5.5$) also reaches the most extreme values with $f_{\rm abs} \approx \{0.21, 0.45, 0.82\}$ when $f_{\rm ion} = \{0.01, 0.1, 1\}$. We emphasize that $f_{\rm abs}$ represents the degree of dust pre-absorption and is therefore indicative of additional dust within ionized regions, which could shrink if on-the-fly dust absorption is included self-consistently. The impact on halo escape fractions is not as large as one might expect based on $f_{\rm abs}$ alone because sightlines with low escape fractions will remain saturated. The global escaped photon rates are most affected if high $f_{\rm esc}$ sightlines also undergo significant dust absorption. Keeping this in mind, our estimates are roughly consistent with other post-processing results from simulations with a multiphase ISM (Kado-Fong et al., 2020; Smith et al., 2021; Tacchella et al., 2021).

In addition to examining the effect of dust on the individual level, we also calculate the change in global escape fractions for different dust survival fractions as summarized in Table 6.1. The dust effect is almost negligible at pre-reionization redshifts ($z \gtrsim 8$). In the most extreme case of full dust ($f_{\rm ion} = 1$), at the end of the simulation ($z = 5.5$) the global escape fraction is reduced to $\approx 43\%$ of the fiducial value from the no-dust scenario. We conclude that dust can be important during the latter half of the reionization process and incorporating on-the-fly prescriptions should be explored further in future simulation models. It remains unclear whether dust mainly adds degeneracy with other parameters such as the birth cloud escape fraction or if there are more fundamental differences.

6.2 Active galactic nuclei

The evident rise in $f_{\rm esc}$ at the high-mass end as seen in Fig. 4-2 suggests the potential presence of efficient ionizing mechanisms beyond the modest increase in stellar mass seen in Fig. 2-1. In particular, AGN formed in massive haloes can create highly energetic jets and significant UV to X-ray radiation. In the context of THESAN, AGN also provide important thermal and kinetic feedback to the surrounding gas (Weinberger et al., 2017). These collectively help generate additional escape channels for ionizing photons. The effects of AGN on reionization have been discussed in some previous studies (e.g. Hassan et al., 2018; Trebitsch et al., 2018; Finkelstein et al., 2019; Dayal et al., 2020), however THESAN offers a unique perspective because AGN sources are included on-the-fly throughout a large simulated volume. Thus, the effects of AGN on galaxies are included in our post-processing MCRT calculations in previous chapters although only stars were considered as photon sources. In this section, we briefly present the results when treating AGN as additional photon sources.

In determining the AGN luminosity, we adopt the AGN spectral energy distribution (SED) from Lusso et al. (2015) with 35.5% of bolometric luminosity (as given in the IllustrisTNG model) contributing to the LyC photons with a sub-grid escape fraction of 100%. We then perform the same MCRT calculations with AGN as the only photon source, assuming isotropic emission and no dust absorption. In the top panel of Fig. 6-2 we show a comparison of the global intrinsic (escaped) photon rate density as dashed (solid) curves between AGN (red) and stars (black) as functions of redshift. The total intrinsic photon rate density $\rho_{\rm int}$ from AGN is negligible at high redshifts, but rapidly rises as z decreases due to the formation of more AGN within massive galaxies. By the end of the simulation at $z = 5.5$, $\rho_{\rm int}$ remains below $2 \times 10^{50}\,\text{photons}\,\text{s}^{-1}\text{cMpc}^{3}$, which is approximately 100 times lower than $\rho_{\rm int}$ from stars. The low contribution from AGN is in agreement with Eide et al. (2020) and is also demonstrated in the original THESAN paper (Kannan et al., 2022). Nevertheless, AGN could potentially increase or even dominate locally in simulations with substantially larger cosmic volumes or different physics modelling.

Similarly, the escaped photon rate density $\rho_{\rm esc}$ from AGN is also negligible, and at $z = 5.5$ reaches global levels that are only about 0.5% of the value from stars. In the bottom panel of Fig. 6-2 we show the corresponding global escape fractions showing that for AGN $f_{\rm esc} \sim 1\%$, which is significantly below that of stars at all times. Contrary to the trend in the stellar $f_{\rm esc}$, which drops slightly as redshift

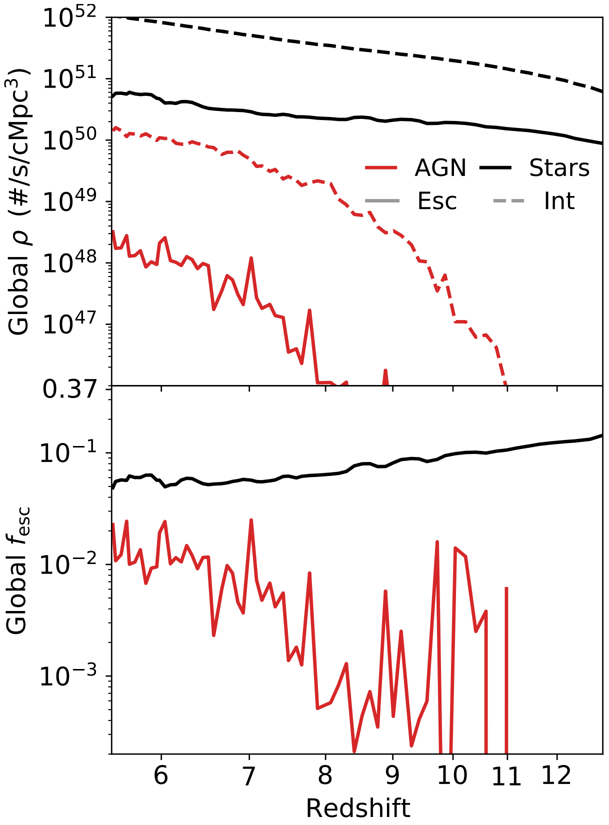

Figure 6-2: *Top:* Global intrinsic (dashed) and escaped (solid) photon rate densities from AGN (red) and stars (black) as functions of redshift. The AGN curves are analogous to Fig. 3-2 but with AGN as the only photon sources. Even at the lowest redshift ($z = 5.5$), AGN only contribute 1% and 0.5% of the total intrinsic and escaped photon rates, respectively. *Bottom:* Comparison of the corresponding global escape fractions for AGN and stars as functions of redshift. AGN $f_{\rm esc}$ are generally much lower than that of stars as a result of being located within galaxy centres. High redshift AGN statistics have large fluctuations due to the lack of massive galaxies in that regime given the limited simulation volume.

decreases, the AGN $f_{\rm esc}$ rises as redshift decreases. The oscillating AGN $f_{\rm esc}$ at high redshifts is due to the lack of statistics. We attribute the relatively low AGN $f_{\rm esc}$ to the fact that AGN are positioned at the centres of galaxy gravitational potential walls, where the abundance of high density gas results in higher self-shielding covering fractions. Thus, escaping from an AGN source requires substantially more ionizing photons to compensate for the systematically larger gas column densities. However, although AGN do not have a significant contribution to the global escaped photons, they potentially play important roles in creating HII regions and ionizing channels for the more diffuse stellar sources.

6.3 Feedback and ISM physics

We now briefly discuss some caveats of the galaxy formation model, which uses a sub-resolution treatment of the ISM as a two-phase gas where cold clumps are embedded in a smooth, hot phase produced by supernova explosions (Springel and Hernquist, 2003). Such subgrid modelling comes with the territory of large-volume simulations with demonstrated agreement with observations down to $z = 0$ (Vogelsberger et al., 2020a), but certainly has implications for ionizing escape fractions. In particular, the temporary decoupling of wind particles from the hydrodynamics reduces the ability to create low density channels through which ionizing radiation can escape (Trebitsch et al., 2017). Additionally, the effective equation of state parametrization is known to result in too smooth of an ISM. The reduced clumpiness compared to simulations that allow the formation of a cold phase leads to high volume-weighted densities in the ISM. This in turn artificially lowers the median escape fractions along with variations across sightlines and haloes.

There may be several different pathways forward to connect sub-resolution physics with large-volume galaxy formation simulations. For example, compressible multi-fluid hydrodynamic schemes can help incorporate multi-scale unresolved phase mixing (Weinberger and Hernquist, 2022) while analytic and tuned prescriptions for cloud-wind interactions can help integrate turbulent mixing and radiative cooling (Fielding and Bryan, 2022). Such effective clumping models may also inform the radiation transport to further our understanding of effective escape fractions through low resolution simulation cells (Buck et al., 2022) or via subgrid clumping factors in coarse-grained reionization simulations (Bianco et al., 2021). However, these may still produce too smooth of an ISM for self-consistent escape fractions from galaxy formation simulations. In fact, approximately converged first principles multi-phase ISM simulations are only feasible for local stellar neighbourhoods and patches of Milky way disks (Kim and Ostriker, 2017; Rathjen et al., 2021) or low-mass dwarf galaxies (Lahén et al., 2020; Steinwandel et al., 2020; Gutcke et al., 2021). We remain optimistic that high-resolution multi-phase zoom-in and small-volume radiation-hydrodynamic simulations can be sufficiently realistic that comparisons to observations also inform us about feedback and ISM physics (Hopkins et al., 2018; Marinacci et al., 2019; Kannan et al., 2020).

Chapter 7

Conclusions

In this work, we have performed Monte Carlo radiative transfer calculations on all haloes from the THESAN simulation to study the production and escape of ionizing photons during the EoR. Our sample consists of haloes in the range $M_{\mathrm{halo}} \in [10^8, 10^{12}]\,\mathrm{M}_\odot$, and covers 90% of haloes with $M_{\mathrm{halo}} > 1.2 \times 10^9\,\mathrm{M}_\odot$ at the midpoint of reionization at $z \approx 7.67$. The THESAN simulations have been shown to produce realistic galaxy and IGM properties that match the current observations and thus provide a self-consistent framework for studying the escape fractions of reionization-era galaxies (Kannan et al., 2022; Garaldi et al., 2022; Smith et al., 2022). The large volume of the simulation ($L_{\mathrm{box}} = 95.5\,\mathrm{cMpc}$) provides rich statistics for massive haloes ($M_{\mathrm{halo}} > 10^{10}\,\mathrm{M}_\odot$) that are important in driving the reionization process but are often statistically underrepresented in previous studies. We summarize our main conclusions in the following points:

1. Lower mass haloes ($\lesssim 10^9\,\mathrm{M}_\odot$) provide the majority of both intrinsic and escaped photons above $z \gtrsim 7$, while more massive haloes ($M_{\mathrm{halo}} \gtrsim 10^{10}\,\mathrm{M}_\odot$) dominate the photon budget thereafter. The most massive haloes ($M_{\mathrm{stars}} \gtrsim 10^9\,\mathrm{M}_\odot$) are particularly important at the later stages of reionization due to their proportionately high intrinsic luminosities. In fact, we find the decrease in the global escape fraction with decreasing redshift can be attributed to this transition from low-to-high mass dominance.

2. Halo escape fractions have a non-trivial dependence on $M_{\rm halo}$: $f_{\rm esc}$ reaches a maximal value of $f_{\rm esc}^{\rm cloud} = 0.37$ for unresolved haloes ($M_{\rm halo} \lesssim 10^8\,{\rm M}_\odot$), meaning that almost all ionizing photons escape after emerging from their local birth clouds. While this agrees with our physical intuition, it is essentially an artefact of numerical resolution in our model and we warn that previous studies reporting high $f_{\rm esc}$ close to the resolution limit of their simulations also likely have this issue. Specifically, the median $f_{\rm esc}$ decreases as halo mass increases, reaching a minimum once haloes are more robustly resolved around $3 \times 10^8\,{\rm M}_\odot$ at $z \lesssim 6$ and $10^9\,{\rm M}_\odot$ at $z \gtrsim 8$. After reaching the minimum value, $f_{\rm esc}$ increases with halo mass, stellar mass, and SFR at all redshifts. This trend still holds even with the presence of dust attenuation, which has a larger effect on massive haloes. We note that while the halo mass corresponding to the minimum $f_{\rm esc}$ shifts as the resolution changes, we find reasonable agreement in the global and resolved halo escape fractions with lower resolution simulations (see Appendix A).

3. Halo $f_{\rm esc}$ are not a simple function of either $M_{\rm halo}$, $M_{\rm stars}$, SFR, or $\Sigma_{\rm SFR}$. However, given a certain halo mass range, galaxies with higher SFR or $\Sigma_{\rm SFR}$ tend to have higher $f_{\rm esc}$. Furthermore, we found by considering SFR, gas mass, and the size of a halo, high $f_{\rm esc}$ can be fairly well distinguished by a theoretical effective SFR surface density $\bar{\Sigma}_{\rm SFR} = {\rm SFR}/M_{\rm gas}/R_{200}^2$.

4. We find a wide range of values for $f_{\rm esc}$ and $\dot{N}_{\rm esc}$ at all redshifts, with lower-mass haloes exhibiting broader distributions than high-mass ones. On the other hand, a tight relation can be observed between intrinsic photon rates and SFR, implying that the large variation of $f_{\rm esc}$ is indeed due to the specific star formation histories and complex environmental dependence.

5. Channels lower escape fractions ($f_{\rm esc}$) have higher hydrogen and helium absorption ($f_{\rm HI}$, $f_{\rm He}$) and correspondingly lower absorption distances ($\langle \ell \rangle$). This implies that the break out of ionizing photons tends to be highly anisotropic. In the case of disk-like galaxies, escape fractions are shown to be higher in face-on directions and essentially zero for edge-on viewing angles. Lower-mass galaxies

tend to be more anisotropic in the sense that half of the escaping flux emerges from a smaller fraction of sightlines and the Gini coefficients are close to unity. The most massive galaxies exhibit a significant trend towards more isotropic and equitable escape.

6. Including dust in the MCRT calculations has observable consequences for high-mass haloes, especially at low redshifts. By the end of the simulation at $z = 5.5$, the global escape fraction decreases from roughly 5% in the no-dust scenario to nearly half that value with the added presence of dust for either the on-the-fly or constant dust-to-metal ratio models.

7. We find that AGN intrinsic LyC production and escape fractions are generally lower than stellar sources. Therefore, while it is important to include AGN in large-volume simulations, they do not contribute significantly to hydrogen reionization.

Our work analyzes millions of resolved galaxies in the large-volume THESAN simulation for haloes with mass between 10^8–$10^{12}\,\mathrm{M}_\odot$. We demonstrate the dominant role of massive haloes in driving cosmic reionization by considering the escaped photons from the ensemble. The escape fraction catalogues will be released as part of the upcoming THESAN public data release, which can be utilized in follow-up analyses. Our results can also be used to inform and calibrate contemporary reionization models. In fact, we argue that including on-the-fly dust absorption is important for simulation volumes with significant numbers of massive haloes ($M_\mathrm{halo} \gtrsim 10^{10}\,\mathrm{M}_\odot$). In the future, we plan to study the time-evolution of f_esc from individual haloes by utilizing merger tree catalogues to correlate the production and escape of ionizing photons with properties of star formation and local environment in greater detail. Furthermore, the THESAN project will soon include high-resolution zoom-in resimulations of a wide range of galaxies including a multiphase ISM framework (Marinacci et al., 2019; Kannan et al., 2020) and self-consistent meso-scale reionization environment inherited directly from the flagship simulation. These efforts will provide additional insights into the physics of escape from reionization-era galaxies and their evolved lower-redshift counterparts for direct comparison to current and upcoming observational data.

Appendix A

Medium resolution simulations

THESAN also includes a suite of medium resolution simulations with different features aiming to investigate the impacts on reionization caused by different physics (Kannan et al., 2022). In this appendix, we analyze the results from several of the medium resolution simulations to compare with the main results from the flagship THESAN-1 simulation explored throughout the body of this paper. In particular, we focus on the THESAN-2 simulation, which has the same initial conditions as THESAN-1 but with two (eight) times lower spatial (mass) resolution. When relevant we also include the THESAN-WC-2 simulation, where the birth cloud escape fraction is slightly higher to compensate for lower star formation in the medium resolution runs. Finally, THESAN-sDAO-2 assumes an alternative dark matter model that includes couplings to relativistic particles giving rise to strong Dark Acoustic Oscillations (sDAOs) cutting off the linear matter power spectrum at small scales. We note that in order to match the observed neutral hydrogen fraction, the different THESAN runs adopt different birth cloud escape fractions $f_{\text{esc}}^{\text{cloud}}$: THESAN-1 and THESAN-2 have $f_{\text{esc}}^{\text{cloud}} = 0.37$, THESAN-WC-2 has $f_{\text{esc}}^{\text{cloud}} = 0.43$, and THESAN-sDAO-2 has $f_{\text{esc}}^{\text{cloud}} = 0.55$.

A.1 Change in global statistics

In Fig. A-1 we show the global escape fractions (solid) as a function of redshift for each of the above-mentioned THESAN variations. The THESAN-1 result is shown in

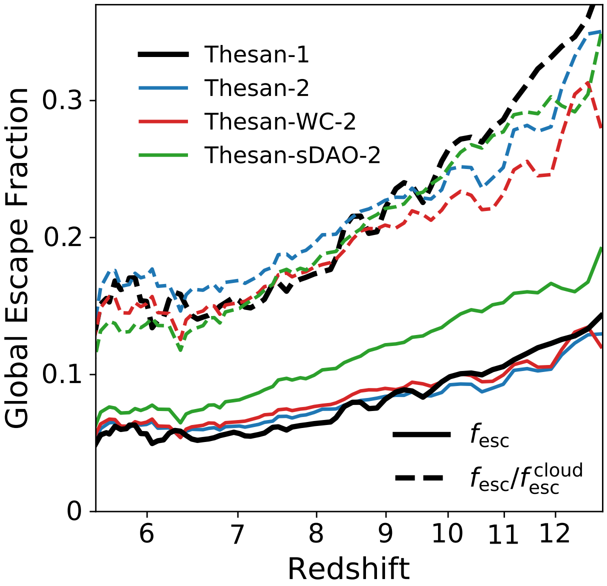

Figure A-1: Comparison of the global photon rate weighted escape fractions from different THESAN simulations (see Fig. 3-2): THESAN-1 (black), THESAN-2 (blue), THESAN-WC-2 (red), and THESAN-sDAO-2 (green). The original escape fractions are shown in solid lines, and the values after normalizing by the birth cloud escape fractions are in dashed lines. Results from all four simulations agree reasonably well after the normalization.

the black curve for comparison (the same as in Fig. 3-2). The dashed lines show the values after normalizing the escape fractions by their birth cloud values to focus on differences in the MCRT calculations. The results from all four simulations are in reasonable agreement after the normalization, implying that the change in mass resolution has relatively little impact on the global result. Thus, the birth cloud escape fraction acts as a viable way to account for the reduced SFR density of the medium resolution runs. Furthermore, the ordering at $z \lesssim 7$ is as expected, i.e. if massive haloes start to dominate and are more or less converged with resolution then the curves should roughly line up near the end of the simulation.

Although the global results remain stable, the change in resolution has a noticeable effect at the low-mass end as higher resolution extends the range for the least massive galaxies modelled. Similar to Fig. 3-3, Fig. A-2 shows the global intrinsic photon rate densities (top), escaped photon rate densities (middle), and escape fractions (bottom) from both THESAN-1 (solid) and THESAN-2 (dashed). At the high-mass end, both

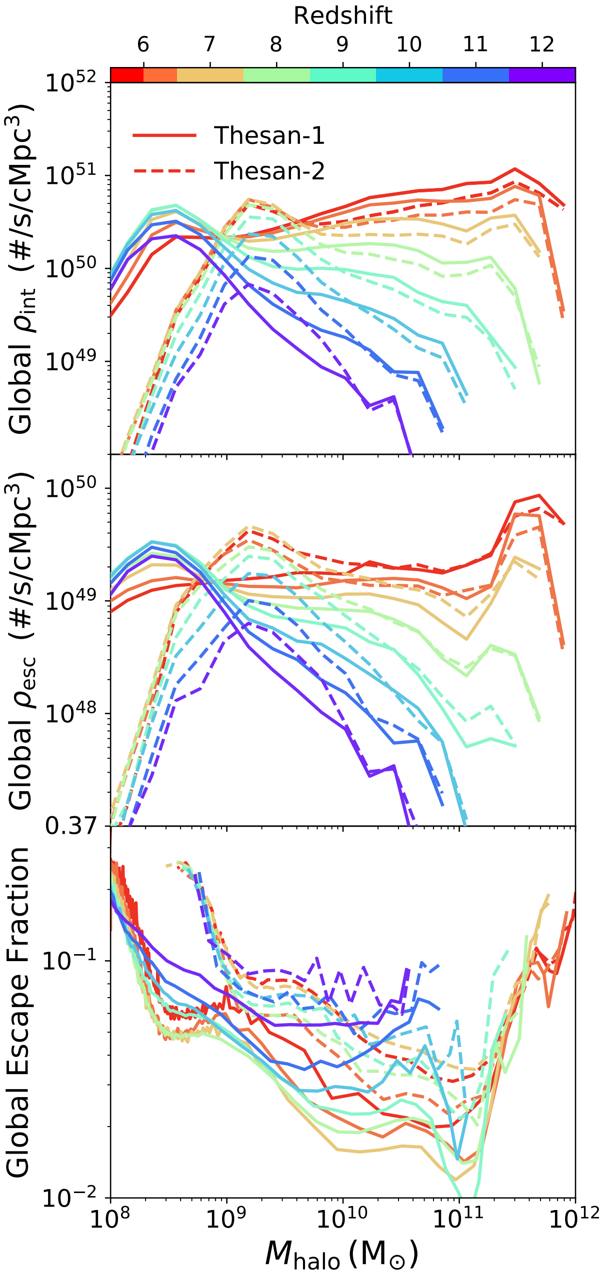

Figure A-2: Resolution comparison between THESAN-1 and THESAN-2 for the global intrinsic $\rho_{\rm int}$ (top) and escaped $\rho_{\rm esc}$ (middle) photon rate densities along with their escape fraction ratio (bottom) as functions of halo mass for several redshift ranges covering $z = 5.5$–13 (see Fig. 3-3). The intrinsic and escaped values in both simulations agree reasonably well at the high-mass end but differ at the low-mass end as halo structures and star-formation histories become poorly resolved. The peaks shift to the lower masses in THESAN-1 as the higher resolution allows the formation of lower mass galaxies. In the bottom panel, THESAN-1 has an overall reduction in global escape fractions across most mass ranges, which is conveniently offset by the higher total intrinsic luminosities, such that there are similar amounts of escaped photons in both scenarios.

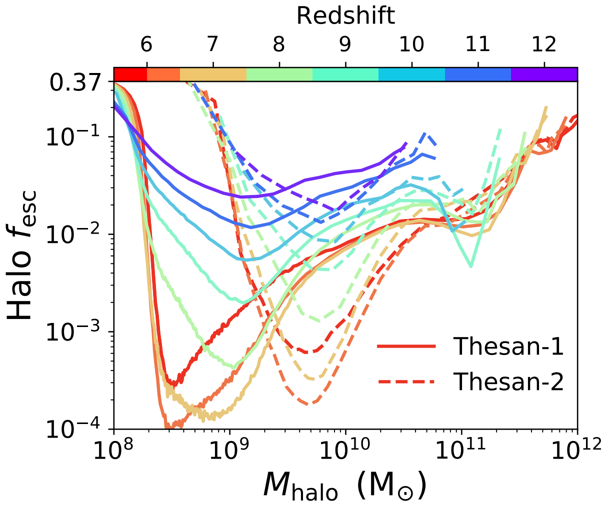

Figure A-3: Resolution comparison between THESAN-1 and THESAN-2 for the median halo values of $f_{\rm esc}$ as a function of $M_{\rm halo}$ across several redshifts in the range $z = 5.5$–13 (see Fig. 4-2). Two simulations admit the same pattern of the $f_{\rm esc}$ dependence on halo mass as discussed in the text with a dip and gradual rise towards more massive haloes. The halo mass at which the minimal $f_{\rm esc}$ occurs increases from $\approx 10^9\,\rm M_\odot$ in THESAN-1 to $\approx 5 \times 10^9\,\rm M_\odot$ in THESAN-2 as the resolution is lowered.

intrinsic and escaped rates have similar values between THESAN-1 and in THESAN-2. The discrepancy between two simulations increases as the mass decreases and resolution artefacts become apparent. The positions of the sharp upturn to maximal escape fractions are entirely set by the resolution, with a shift to the left as more low-mass galaxies are being resolved in THESAN-1. In terms of global escape fractions, THESAN-1 has overall lower values, which can be understood by requiring the total amount of photons to be the same for both simulations to have a consistent description of the reionization history. Therefore, the higher total luminosity in THESAN-1 due to a larger number of resolved stars is compensated by lower global escape fractions. We conclude that the global escaped photon rate densities in THESAN-1 and THESAN-2 are reasonably converged for the dominant drivers of reionization ($M_{\rm halo} \gtrsim 10^{10}\,\rm M_\odot$).

A.2 Change in individual halo dependence

We also argue that the change in resolution does not significantly alter the pattern of the halo median $f_{\rm esc}$ dependence on halo mass. As shown in Fig. A-3, the $f_{\rm esc}$

dependence on $M_{\rm halo}$ in THESAN-2 resembles the result from THESAN-1 except that the dip marking the transition from low completeness of low-mass haloes and sufficient resolution for richer substructures is shifted to higher masses. This dip and gradual rise of $f_{\rm esc}$ towards more massive haloes corresponds to $\approx 10^9\,{\rm M}_\odot$ in THESAN-1 to $\approx 5 \times 10^9\,{\rm M}_\odot$ in THESAN-2, again due to resolution effects. Overall, it is clear that the resolution requirements for obtaining robust halo escape fractions are likely more demanding than for other galaxy formation properties such as SFRs or gas fractions.

Bibliography

Angulo, R. E. and Pontzen, A. (2016). Cosmological N-body simulations with suppressed variance. , 462(1):L1–L5.

Barkana, R. and Loeb, A. (2001). In the beginning: the first sources of light and the reionization of the universe. , 349(2):125–238.

Barnes, J. and Hut, P. (1986). A hierarchical O(N log N) force-calculation algorithm. , 324(6096):446–449.

Bianco, M., Iliev, I. T., Ahn, K., Giri, S. K., Mao, Y., Park, H., and Shapiro, P. R. (2021). The impact of inhomogeneous subgrid clumping on cosmic reionization - II. Modelling stochasticity. , 504(2):2443–2460.

Bridge, C. R., Teplitz, H. I., Siana, B., Scarlata, C., Conselice, C. J., Ferguson, H. C., Brown, T. M., Salvato, M., Rudie, G. C., de Mello, D. F., Colbert, J., Gardner, J. P., Giavalisco, M., and Armus, L. (2010). A Spectroscopic Search for Leaking Lyman Continuum at z ~0.7. , 720(1):465–479.

Bromm, V. and Yoshida, N. (2011). The First Galaxies. , 49(1):373–407.

Buck, T., Pfrommer, C., Girichidis, P., and Corobean, B. (2022). Escaping the maze: a statistical sub-grid model for cloud-scale density structures in the interstellar medium. .

Cen, R. and Kimm, T. (2015). Quantifying Distributions of the Lyman Continuum Escape Fraction. , 801(2):L25.

Chabrier, G. (2003). The Galactic Disk Mass Function: Reconciliation of the Hubble Space Telescope and Nearby Determinations. , 586(2):L133–L136.

Davies, F. B., Hennawi, J. F., Bañados, E., Lukić, Z., Decarli, R., Fan, X., Farina, E. P., Mazzucchelli, C., Rix, H.-W., Venemans, B. P., Walter, F., Wang, F., and Yang, J. (2018). Quantitative Constraints on the Reionization History from the IGM Damping Wing Signature in Two Quasars at z > 7. , 864(2):142.

Dawoodbhoy, T., Shapiro, P. R., Ocvirk, P., Aubert, D., Gillet, N., Choi, J.-H., Iliev, I. T., Teyssier, R., Yepes, G., Gottlöber, S., D'Aloisio, A., Park, H., and Hoffman, Y. (2018). Suppression of star formation in low-mass galaxies caused by the reionization of their local neighbourhood. , 480(2):1740–1753.

Dayal, P., Volonteri, M., Choudhury, T. R., Schneider, R., Trebitsch, M., Gnedin, N. Y., Atek, H., Hirschmann, M., and Reines, A. (2020). Reionization with galaxies and active galactic nuclei. , 495(3):3065–3078.

Draine, B. T. (2011). On Radiation Pressure in Static, Dusty H II Regions. , 732(2):100.

Eide, M. B., Ciardi, B., Graziani, L., Busch, P., Feng, Y., and Di Matteo, T. (2020). Large-scale simulations of H and He reionization and heating driven by stars and more energetic sources. , 498(4):6083–6099.

Eldridge, J. J., Stanway, E. R., Xiao, L., McClelland, L. A. S., Taylor, G., Ng, M., Greis, S. M. L., and Bray, J. C. (2017). Binary Population and Spectral Synthesis Version 2.1: Construction, Observational Verification, and New Results. , 34:e058.

Faucher-Giguère, C.-A. (2020). A cosmic UV/X-ray background model update. , 493(2):1614–1632.

Fielding, D. B. and Bryan, G. L. (2022). The Structure of Multiphase Galactic Winds. , 924(2):82.

Finkelstein, S. L., D'Aloisio, A., Paardekooper, J.-P., Ryan, Russell, J., Behroozi, P., Finlator, K., Livermore, R., Upton Sanderbeck, P. R., Dalla Vecchia, C., and Khochfar, S. (2019). Conditions for Reionizing the Universe with a Low Galaxy Ionizing Photon Escape Fraction. , 879(1):36.

Finkelstein, S. L., Papovich, C., Ryan, R. E., Pawlik, A. H., Dickinson, M., Ferguson, H. C., Finlator, K., Koekemoer, A. M., Giavalisco, M., Cooray, A., Dunlop, J. S., Faber, S. M., Grogin, N. A., Kocevski, D. D., and Newman, J. A. (2012). CANDELS: The Contribution of the Observed Galaxy Population to Cosmic Reionization. , 758(2):93.

Flury, S. R., Jaskot, A. E., Ferguson, H. C., Worseck, G., Makan, K., Chisholm, J., Saldana-Lopez, A., Schaerer, D., McCandless, S., Wang, B., Ford, N. M., Heckman, T., Ji, Z., Giavalisco, M., Amorin, R., Atek, H., Blaizot, J., Borthakur, S., Carr, C., Castellano, M., Cristiani, S., de Barros, S., Dickinson, M., Finkelstein, S. L., Fleming, B., Fontanot, F., Garel, T., Grazian, A., Hayes, M., Henry, A., Mauerhofer, V., Micheva, G., Oey, M. S., Ostlin, G., Papovich, C., Pentericci, L., Ravindranath, S., Rosdahl, J., Rutkowski, M., Santini, P., Scarlata, C., Teplitz, H., Thuan, T., Trebitsch, M., Vanzella, E., Verhamme, A., and Xu, X. (2022). The Low-Redshift Lyman Continuum Survey I: New, Diverse Local Lyman-Continuum Emitters. *arXiv e-prints*, page arXiv:2201.11716.

Garaldi, E., Kannan, R., Smith, A., Springel, V., Pakmor, R., Vogelsberger, M., and Hernquist, L. (2022). The THESAN project: properties of the intergalactic medium and its connection to reionization-era galaxies. , 512(4):4909–4933.

Genel, S., Bryan, G. L., Springel, V., Hernquist, L., Nelson, D., Pillepich, A., Weinberger, R., Pakmor, R., Marinacci, F., and Vogelsberger, M. (2019). A Quantification of the Butterfly Effect in Cosmological Simulations and Implications for Galaxy Scaling Relations. , 871(1):21.

Gnedin, N. Y. (2014). Cosmic Reionization on Computers. I. Design and Calibration of Simulations. , 793(1):29.

Gnedin, N. Y., Kravtsov, A. V., and Chen, H.-W. (2008). Escape of Ionizing Radiation from High-Redshift Galaxies. , 672(2):765–775.

Grazian, A., Giallongo, E., Paris, D., Boutsia, K., Dickinson, M., Santini, P., Windhorst, R. A., Jansen, R. A., Cohen, S. H., Ashcraft, T. A., Scarlata, C., Rutkowski, M. J., Vanzella, E., Cusano, F., Cristiani, S., Giavalisco, M., Ferguson, H. C., Koekemoer, A., Grogin, N. A., Castellano, M., Fiore, F., Fontana, A., Marchi, F., Pedichini, F., Pentericci, L., Amorín, R., Barro, G., Bonchi, A., Bongiorno, A., Faber, S. M., Fumana, M., Galametz, A., Guaita, L., Kocevski, D. D., Merlin, E., Nonino, M., O'Connell, R. W., Pilo, S., Ryan, R. E., Sani, E., Speziali, R., Testa, V., Weiner, B., and Yan, H. (2017). Lyman continuum escape fraction of faint galaxies at z 3.3 in the CANDELS/GOODS-North, EGS, and COSMOS fields with LBC. , 602:A18.

Greig, B., Mesinger, A., Haiman, Z., and Simcoe, R. A. (2017). Are we witnessing the epoch of reionisation at z = 7.1 from the spectrum of J1120+0641? , 466(4):4239–4249.

Gutcke, T. A., Pakmor, R., Naab, T., and Springel, V. (2021). LYRA - I. Simulating the multiphase ISM of a dwarf galaxy with variable energy supernovae from individual stars. , 501(4):5597–5615.

Haardt, F. and Madau, P. (2012). Radiative Transfer in a Clumpy Universe. IV. New Synthesis Models of the Cosmic UV/X-Ray Background. , 746(2):125.

Hassan, S., Davé, R., Mitra, S., Finlator, K., Ciardi, B., and Santos, M. G. (2018). Constraining the contribution of active galactic nuclei to reionization. , 473(1):227–240.

Hoang, T., Tram, L. N., Lee, H., and Ahn, S.-H. (2019). Rotational disruption of dust grains by radiative torques in strong radiation fields. *Nature Astronomy*, 3:766–775.

Hopkins, P. F., Wetzel, A., Kereš, D., Faucher-Giguère, C.-A., Quataert, E., Boylan-Kolchin, M., Murray, N., Hayward, C. C., Garrison-Kimmel, S., Hummels, C., Feldmann, R., Torrey, P., Ma, X., Anglés-Alcázar, D., Su, K.-Y., Orr, M., Schmitz, D., Escala, I., Sanderson, R., Grudić, M. Y., Hafen, Z., Kim, J.-H., Fitts, A., Bullock, J. S., Wheeler, C., Chan, T. K., Elbert, O. D., and Narayanan, D. (2018). FIRE-2 simulations: physics versus numerics in galaxy formation. , 480(1):800–863.

Hu, C.-Y., Zhukovska, S., Somerville, R. S., and Naab, T. (2019). Thermal and non-thermal dust sputtering in hydrodynamical simulations of the multiphase interstellar medium. , 487(3):3252–3269.

Iyer, K. G., Tacchella, S., Genel, S., Hayward, C. C., Hernquist, L., Brooks, A. M., Caplar, N., Davé, R., Diemer, B., Forbes, J. C., Gawiser, E., Somerville, R. S., and Starkenburg, T. K. (2020). The diversity and variability of star formation histories in models of galaxy evolution. , 498(1):430–463.

Izotov, Y. I., Schaerer, D., Worseck, G., Guseva, N. G., Thuan, T. X., Verhamme, A., Orlitová, I., and Fricke, K. J. (2018). J1154+2443: a low-redshift compact star-forming galaxy with a 46 per cent leakage of Lyman continuum photons. , 474(4):4514–4527.

Japelj, J., Vanzella, E., Fontanot, F., Cristiani, S., Caminha, G. B., Tozzi, P., Balestra, I., Rosati, P., and Meneghetti, M. (2017). Constraints on the Lyman continuum escape fraction for faint star-forming galaxies. , 468(1):389–403.

Kado-Fong, E., Kim, J.-G., Ostriker, E. C., and Kim, C.-G. (2020). Diffuse Ionized Gas in Simulations of Multiphase, Star-forming Galactic Disks. , 897(2):143.

Kannan, R., Garaldi, E., Smith, A., Pakmor, R., Springel, V., Vogelsberger, M., and Hernquist, L. (2022). Introducing the THESAN project: radiation-magnetohydrodynamic simulations of the epoch of reionization. , 511(3):4005–4030.

Kannan, R., Marinacci, F., Vogelsberger, M., Sales, L. V., Torrey, P., Springel, V., and Hernquist, L. (2020). Simulating the interstellar medium of galaxies with radiative transfer, non-equilibrium thermochemistry, and dust. , 499(4):5732–5748.

Kannan, R., Smith, A., Garaldi, E., Shen, X., Vogelsberger, M., Pakmor, R., Springel, V., and Hernquist, L. (2021). The THESAN project: predictions for multi-tracer line intensity mapping in the Epoch of Reionization. *arXiv e-prints*, page arXiv:2111.02411.

Kannan, R., Vogelsberger, M., Marinacci, F., McKinnon, R., Pakmor, R., and Springel, V. (2019). AREPO-RT: radiation hydrodynamics on a moving mesh. , 485(1):117–149.

Kim, C.-G. and Ostriker, E. C. (2017). Three-phase Interstellar Medium in Galaxies Resolving Evolution with Star Formation and Supernova Feedback (TIGRESS): Algorithms, Fiducial Model, and Convergence. , 846(2):133.

Kimm, T., Katz, H., Haehnelt, M., Rosdahl, J., Devriendt, J., and Slyz, A. (2017). Feedback-regulated star formation and escape of LyC photons from mini-haloes during reionization. , 466(4):4826–4846.

Kulkarni, G., Keating, L. C., Haehnelt, M. G., Bosman, S. E. I., Puchwein, E., Chardin, J., and Aubert, D. (2019). Large Ly α opacity fluctuations and low CMB

τ in models of late reionization with large islands of neutral hydrogen extending to z $<$ 5.5. , 485(1):L24–L28.

Lahén, N., Naab, T., Johansson, P. H., Elmegreen, B., Hu, C.-Y., Walch, S., Steinwandel, U. P., and Moster, B. P. (2020). The GRIFFIN Project—Formation of Star Clusters with Individual Massive Stars in a Simulated Dwarf Galaxy Starburst. , 891(1):2.

Laursen, P., Sommer-Larsen, J., and Andersen, A. C. (2009). Lyα Radiative Transfer with Dust: Escape Fractions from Simulated High-Redshift Galaxies. , 704(2):1640–1656.

Levermore, C. D. (1984). Relating Eddington factors to flux limiters. , 31(2):149–160.

Loeb, A. and Furlanetto, S. R. (2013). *The First Galaxies in the Universe*. Princeton Univ. Press, Princeton, NJ.

Lusso, E., Worseck, G., Hennawi, J. F., Prochaska, J. X., Vignali, C., Stern, J., and O'Meara, J. M. (2015). The first ultraviolet quasar-stacked spectrum at z 2.4 from WFC3. , 449(4):4204–4220.

Ma, Q.-B., Fiaschi, S., Ciardi, B., Busch, P., and Eide, M. B. (2022). A CRASH simulation of the contribution of binary stars to the epoch of reionization. .

Ma, X., Hopkins, P. F., Kasen, D., Quataert, E., Faucher-Giguère, C.-A., Kereš, D., Murray, N., and Strom, A. (2016). Binary stars can provide the 'missing photons' needed for reionization. , 459(4):3614–3619.

Ma, X., Kasen, D., Hopkins, P. F., Faucher-Giguère, C.-A., Quataert, E., Kereš, D., and Murray, N. (2015). The difficulty of getting high escape fractions of ionizing photons from high-redshift galaxies: a view from the FIRE cosmological simulations. , 453(1):960–975.

Ma, X., Quataert, E., Wetzel, A., Faucher-Giguère, C.-A., and Boylan-Kolchin, M. (2021). The contribution of globular clusters to cosmic reionization. , 504(3):4062–4071.

Ma, X., Quataert, E., Wetzel, A., Hopkins, P. F., Faucher-Giguère, C.-A., and Kereš, D. (2020). No missing photons for reionization: moderate ionizing photon escape fractions from the FIRE-2 simulations. , 498(2):2001–2017.

Madau, P. (2017). Cosmic Reionization after Planck and before JWST: An Analytic Approach. , 851(1):50.

Madau, P., Haardt, F., and Rees, M. J. (1999). Radiative Transfer in a Clumpy Universe. III. The Nature of Cosmological Ionizing Sources. , 514(2):648–659.

Marinacci, F., Sales, L. V., Vogelsberger, M., Torrey, P., and Springel, V. (2019). Simulating the interstellar medium and stellar feedback on a moving mesh: implementation and isolated galaxies. , 489(3):4233–4260.

Marinacci, F., Vogelsberger, M., Pakmor, R., Torrey, P., Springel, V., Hernquist, L., Nelson, D., Weinberger, R., Pillepich, A., Naiman, J., and Genel, S. (2018). First results from the IllustrisTNG simulations: radio haloes and magnetic fields. , 480(4):5113–5139.

Mason, C. A., Fontana, A., Treu, T., Schmidt, K. B., Hoag, A., Abramson, L., Amorin, R., Bradač, M., Guaita, L., Jones, T., Henry, A., Malkan, M. A., Pentericci, L., Trenti, M., and Vanzella, E. (2019). Inferences on the timeline of reionization at z $\sim$ 8 from the KMOS Lens-Amplified Spectroscopic Survey. , 485(3):3947–3969.

McGreer, I. D., Mesinger, A., and D'Odorico, V. (2015). Model-independent evidence in favour of an end to reionization by z $\approx$ 6. , 447(1):499–505.

McKinnon, R., Torrey, P., Vogelsberger, M., Hayward, C. C., and Marinacci, F. (2017). Simulating the dust content of galaxies: successes and failures. , 468(2):1505–1521.

Naidu, R. P., Tacchella, S., Mason, C. A., Bose, S., Oesch, P. A., and Conroy, C. (2020). Rapid Reionization by the Oligarchs: The Case for Massive, UV-bright, Star-forming Galaxies with High Escape Fractions. , 892(2):109.

Naiman, J. P., Pillepich, A., Springel, V., Ramirez-Ruiz, E., Torrey, P., Vogelsberger, M., Pakmor, R., Nelson, D., Marinacci, F., Hernquist, L., Weinberger, R., and Genel, S. (2018). First results from the IllustrisTNG simulations: a tale of two elements - chemical evolution of magnesium and europium. , 477(1):1206–1224.

Nelson, D., Pillepich, A., Springel, V., Pakmor, R., Weinberger, R., Genel, S., Torrey, P., Vogelsberger, M., Marinacci, F., and Hernquist, L. (2019). First results from the TNG50 simulation: galactic outflows driven by supernovae and black hole feedback. , 490(3):3234–3261.

Nelson, D., Pillepich, A., Springel, V., Weinberger, R., Hernquist, L., Pakmor, R., Genel, S., Torrey, P., Vogelsberger, M., Kauffmann, G., Marinacci, F., and Naiman, J. (2018). First results from the IllustrisTNG simulations: the galaxy colour bimodality. , 475(1):624–647.

Nestor, D. B., Shapley, A. E., Kornei, K. A., Steidel, C. C., and Siana, B. (2013). A Refined Estimate of the Ionizing Emissivity from Galaxies at z ~= 3: Spectroscopic Follow-up in the SSA22a Field. , 765(1):47.

Paardekooper, J. P., Khochfar, S., and Dalla, C. V. (2013). The first billion years project: proto-galaxies reionizing the universe. , 429:L94–L98.

Paardekooper, J.-P., Khochfar, S., and Dalla Vecchia, C. (2015). The First Billion Years project: the escape fraction of ionizing photons in the epoch of reionization. , 451(3):2544–2563.

Pahl, A. J., Shapley, A., Steidel, C. C., Chen, Y., and Reddy, N. A. (2021). An uncontaminated measurement of the escaping Lyman continuum at z 3. , 505(2):2447–2467.

Pahl, A. J., Shapley, A., Steidel, C. C., Reddy, N. A., and Chen, Y. (2022). Searching for the connection between ionizing-photon escape and the surface density of star formation at z~3. *arXiv e-prints*, page arXiv:2202.00016.

Pillepich, A., Nelson, D., Hernquist, L., Springel, V., Pakmor, R., Torrey, P., Weinberger, R., Genel, S., Naiman, J. P., Marinacci, F., and Vogelsberger, M. (2018a). First results from the IllustrisTNG simulations: the stellar mass content of groups and clusters of galaxies. , 475(1):648–675.

Pillepich, A., Nelson, D., Springel, V., Pakmor, R., Torrey, P., Weinberger, R., Vogelsberger, M., Marinacci, F., Genel, S., van der Wel, A., and Hernquist, L. (2019). First results from the TNG50 simulation: the evolution of stellar and gaseous discs across cosmic time. , 490(3):3196–3233.

Pillepich, A., Springel, V., Nelson, D., Genel, S., Naiman, J., Pakmor, R., Hernquist, L., Torrey, P., Vogelsberger, M., Weinberger, R., and Marinacci, F. (2018b). Simulating galaxy formation with the IllustrisTNG model. , 473(3):4077–4106.

Planck Collaboration, Ade, P. A. R., Aghanim, N., Arnaud, M., Ashdown, M., Aumont, J., Baccigalupi, C., Banday, A. J., Barreiro, R. B., Bartlett, J. G., Bartolo, N., Battaner, E., Battye, R., Benabed, K., Benoît, A., Benoit-Lévy, A., Bernard, J. P., Bersanelli, M., Bielewicz, P., Bock, J. J., Bonaldi, A., Bonavera, L., Bond, J. R., Borrill, J., Bouchet, F. R., Boulanger, F., Bucher, M., Burigana, C., Butler, R. C., Calabrese, E., Cardoso, J. F., Catalano, A., Challinor, A., Chamballu, A., Chary, R. R., Chiang, H. C., Chluba, J., Christensen, P. R., Church, S., Clements, D. L., Colombi, S., Colombo, L. P. L., Combet, C., Coulais, A., Crill, B. P., Curto, A., Cuttaia, F., Danese, L., Davies, R. D., Davis, R. J., de Bernardis, P., de Rosa, A., de Zotti, G., Delabrouille, J., Désert, F. X., Di Valentino, E., Dickinson, C., Diego, J. M., Dolag, K., Dole, H., Donzelli, S., Doré, O., Douspis, M., Ducout, A., Dunkley, J., Dupac, X., Efstathiou, G., Elsner, F., Enßlin, T. A., Eriksen, H. K., Farhang, M., Fergusson, J., Finelli, F., Forni, O., Frailis, M., Fraisse, A. A., Franceschi, E., Frejsel, A., Galeotta, S., Galli, S., Ganga, K., Gauthier, C., Gerbino, M., Ghosh, T., Giard, M., Giraud-Héraud, Y., Giusarma, E., Gjerløw, E., González-Nuevo, J., Górski, K. M., Gratton, S., Gregorio, A., Gruppuso, A., Gudmundsson, J. E., Hamann, J., Hansen, F. K., Hanson, D., Harrison, D. L., Helou, G., Henrot-Versillé, S., Hernández-Monteagudo, C., Herranz, D., Hildebrand t, S. R., Hivon, E., Hobson, M., Holmes, W. A., Hornstrup, A., Hovest, W., Huang, Z., Huffenberger, K. M., Hurier, G., Jaffe, A. H., Jaffe, T. R., Jones, W. C., Juvela, M., Keihänen, E., Keskitalo, R., Kisner, T. S., Kneissl, R., Knoche, J., Knox, L., Kunz, M., Kurki-Suonio, H., Lagache, G., Lähteenmäki, A., Lamarre, J. M., Lasenby, A., Lattanzi, M., Lawrence, C. R., Leahy, J. P., Leonardi, R., Lesgourgues, J., Levrier, F., Lewis, A., Liguori, M., Lilje, P. B., Linden-Vørnle, M., López-Caniego, M., Lubin, P. M., Macías-Pérez, J. F., Maggio, G., Maino, D., Mandolesi, N., Mangilli, A., Marchini, A., Maris, M., Martin, P. G., Martinelli, M., Martínez-González, E., Masi, S., Matarrese, S., McGehee, P., Meinhold, P. R., Melchiorri, A., Melin, J. B., Mendes, L., Mennella, A., Migliaccio, M., Millea, M., Mitra, S., Miville-Deschênes, M. A., Moneti, A., Montier, L., Morgante, G., Mortlock, D., Moss, A., Munshi, D., Murphy, J. A., Naselsky, P., Nati, F., Natoli, P., Netterfield, C. B., Nørgaard-Nielsen, H. U., Noviello, F., Novikov, D., Novikov, I., Oxborrow, C. A., Paci, F., Pagano, L., Pajot, F., Paladini, R., Paoletti, D., Partridge, B., Pasian, F., Patanchon, G., Pearson, T. J., Perdereau, O., Perotto, L., Perrotta, F., Pettorino, V., Piacentini, F., Piat, M., Pierpaoli, E., Pietrobon, D., Plaszczynski, S., Pointecouteau, E., Polenta, G., Popa, L., Pratt, G. W., Prézeau, G., Prunet, S., Puget, J. L., Rachen, J. P., Reach, W. T., Rebolo, R., Reinecke, M., Remazeilles, M., Renault, C., Renzi, A., Ristorcelli, I., Rocha, G., Rosset, C., Rossetti, M., Roudier, G., Rouillé d'Orfeuil, B., Rowan-Robinson, M., Rubiño-Martín, J. A., Rusholme, B., Said, N., Salvatelli, V., Salvati, L., Sandri, M., Santos, D., Savelainen, M., Savini, G., Scott, D., Seiffert, M. D., Serra, P., Shellard, E. P. S., Spencer, L. D., Spinelli, M., Stolyarov, V., Stompor, R., Sudiwala, R., Sunyaev, R., Sutton, D., Suur-Uski, A. S., Sygnet, J. F., Tauber, J. A., Terenzi, L., Toffolatti, L., Tomasi, M., Tristram, M., Trombetti, T., Tucci, M., Tuovinen, J., Türler, M., Umana, G., Valenziano, L., Valiviita, J., Van Tent, F., Vielva, P., Villa, F., Wade, L. A., Wandelt, B. D., Wehus, I. K., White, M., White, S. D. M., Wilkinson, A., Yvon, D., Zacchei, A., and Zonca, A. (2016). Planck 2015 results. XIII. Cosmological parameters. , 594:A13.

Planck Collaboration, Aghanim, N., Akrami, Y., Ashdown, M., Aumont, J., Baccigalupi, C., Ballardini, M., Banday, A. J., Barreiro, R. B., Bartolo, N., Basak, S., Battye, R., Benabed, K., Bernard, J. P., Bersanelli, M., Bielewicz, P., Bock, J. J., Bond, J. R., Borrill, J., Bouchet, F. R., Boulanger, F., Bucher, M., Burigana, C., Butler, R. C., Calabrese, E., Cardoso, J. F., Carron, J., Challinor, A., Chiang, H. C., Chluba, J., Colombo, L. P. L., Combet, C., Contreras, D., Crill, B. P., Cuttaia, F., de Bernardis, P., de Zotti, G., Delabrouille, J., Delouis, J. M., Di Valentino, E., Diego, J. M., Doré, O., Douspis, M., Ducout, A., Dupac, X., Dusini, S., Efstathiou, G., Elsner, F., Enßlin, T. A., Eriksen, H. K., Fantaye, Y., Farhang, M., Fergusson, J., Fernandez-Cobos, R., Finelli, F., Forastieri, F., Frailis, M., Fraisse, A. A., Franceschi, E., Frolov, A., Galeotta, S., Galli, S., Ganga, K., Génova-Santos, R. T., Gerbino, M., Ghosh, T., González-Nuevo, J., Górski, K. M., Gratton, S., Gruppuso, A., Gudmundsson, J. E., Hamann, J., Handley, W., Hansen, F. K., Herranz, D., Hildebrandt, S. R., Hivon, E., Huang, Z., Jaffe, A. H., Jones, W. C., Karakci, A., Keihänen, E., Keskitalo, R., Kiiveri, K., Kim, J., Kisner, T. S., Knox, L., Krachmalnicoff, N., Kunz, M., Kurki-Suonio, H., Lagache, G., Lamarre, J. M., Lasenby, A., Lattanzi, M., Lawrence, C. R., Le Jeune, M., Lemos, P., Lesgourgues, J., Levrier, F., Lewis, A., Liguori, M., Lilje, P. B., Lilley, M., Lindholm, V., López-Caniego, M., Lubin, P. M., Ma, Y. Z., Macías-Pérez, J. F., Maggio, G., Maino, D., Mandolesi, N., Mangilli, A., Marcos-Caballero, A., Maris, M., Martin, P. G., Martinelli, M., Martínez-González, E., Matarrese, S., Mauri, N., McEwen,

J. D., Meinhold, P. R., Melchiorri, A., Mennella, A., Migliaccio, M., Millea, M., Mitra, S., Miville-Deschênes, M. A., Molinari, D., Montier, L., Morgante, G., Moss, A., Natoli, P., Nørgaard-Nielsen, H. U., Pagano, L., Paoletti, D., Partridge, B., Patanchon, G., Peiris, H. V., Perrotta, F., Pettorino, V., Piacentini, F., Polastri, L., Polenta, G., Puget, J. L., Rachen, J. P., Reinecke, M., Remazeilles, M., Renzi, A., Rocha, G., Rosset, C., Roudier, G., Rubiño-Martín, J. A., Ruiz-Granados, B., Salvati, L., Sandri, M., Savelainen, M., Scott, D., Shellard, E. P. S., Sirignano, C., Sirri, G., Spencer, L. D., Sunyaev, R., Suur-Uski, A. S., Tauber, J. A., Tavagnacco, D., Tenti, M., Toffolatti, L., Tomasi, M., Trombetti, T., Valenziano, L., Valiviita, J., Van Tent, B., Vibert, L., Vielva, P., Villa, F., Vittorio, N., Wandelt, B. D., Wehus, I. K., White, M., White, S. D. M., Zacchei, A., and Zonca, A. (2020). Planck 2018 results. VI. Cosmological parameters. , 641:A6.

Puglisi, A., Rodighiero, G., Franceschini, A., Talia, M., Cimatti, A., Baronchelli, I., Daddi, E., Renzini, A., Schawinski, K., Mancini, C., Silverman, J., Gruppioni, C., Lutz, D., Berta, S., and Oliver, S. J. (2016). Dust attenuation in z ~1 galaxies from Herschel and 3D-HST Hα measurements. , 586:A83.

Rathjen, T.-E., Naab, T., Girichidis, P., Walch, S., Wünsch, R., Dinnbier, F., Seifried, D., Klessen, R. S., and Glover, S. C. O. (2021). SILCC VI - Multiphase ISM structure, stellar clustering, and outflows with supernovae, stellar winds, ionizing radiation, and cosmic rays. , 504(1):1039–1061.

Rivera-Thorsen, T. E., Dahle, H., Chisholm, J., Florian, M. K., Gronke, M., Rigby, J. R., Gladders, M. D., Mahler, G., Sharon, K., and Bayliss, M. (2019). Gravitational lensing reveals ionizing ultraviolet photons escaping from a distant galaxy. *Science*, 366(6466):738–741.

Robertson, B. E., Ellis, R. S., Dunlop, J. S., McLure, R. J., and Stark, D. P. (2010). Early star-forming galaxies and the reionization of the Universe. , 468(7320):49–55.

Robertson, B. E., Ellis, R. S., Furlanetto, S. R., and Dunlop, J. S. (2015). Cosmic Reionization and Early Star-forming Galaxies: A Joint Analysis of New Constraints from Planck and the Hubble Space Telescope. , 802(2):L19.

Robertson, B. E., Furlanetto, S. R., Schneider, E., Charlot, S., Ellis, R. S., Stark, D. P., McLure, R. J., Dunlop, J. S., Koekemoer, A., Schenker, M. A., Ouchi, M., Ono, Y., Curtis-Lake, E., Rogers, A. B., Bowler, R. A. A., and Cirasuolo, M. (2013). New Constraints on Cosmic Reionization from the 2012 Hubble Ultra Deep Field Campaign. , 768(1):71.

Rosdahl, J., Katz, H., Blaizot, J., Kimm, T., Michel-Dansac, L., Garel, T., Haehnelt, M., Ocvirk, P., and Teyssier, R. (2018). The SPHINX cosmological simulations of the first billion years: the impact of binary stars on reionization. , 479(1):994–1016.

Rutkowski, M. J., Scarlata, C., Haardt, F., Siana, B., Henry, A., Rafelski, M., Hayes, M., Salvato, M., Pahl, A. J., Mehta, V., Beck, M., Malkan, M., and Teplitz, H. I.

(2016). Lyman Continuum Escape Fraction of Star-forming Dwarf Galaxies at z $\sim$ 1. , 819(1):81.

Rybicki, G. B. and Lightman, A. P. (1986). *Radiative Processes in Astrophysics.*

Saldana-Lopez, A., Schaerer, D., Chisholm, J., Flury, S. R., Jaskot, A. E., Worseck, G., Makan, K., Gazagnes, S., Mauerhofer, V., Verhamme, A., Amorín, R. O., Ferguson, H. C., Giavalisco, M., Grazian, A., Hayes, M. J., Heckman, T. M., Henry, A., Ji, Z., Marques-Chaves, R., McCandliss, S. R., Oey, M. S., Östlin, G., Pentericci, L., Thuan, T. X., Trebitsch, M., Vanzella, E., and Xu, X. (2022). The Low-Redshift Lyman Continuum Survey. Unveiling the ISM properties of low-z Lyman continuum emitters. *arXiv e-prints*, page arXiv:2201.11800.

Schenker, M. A., Ellis, R. S., Konidaris, N. P., and Stark, D. P. (2014). Line-emitting Galaxies beyond a Redshift of 7: An Improved Method for Estimating the Evolving Neutrality of the Intergalactic Medium. , 795(1):20.

Siana, B., Teplitz, H. I., Ferguson, H. C., Brown, T. M., Giavalisco, M., Dickinson, M., Chary, R.-R., de Mello, D. F., Conselice, C. J., Bridge, C. R., Gardner, J. P., Colbert, J. W., and Scarlata, C. (2010). A Deep Hubble Space Telescope Search for Escaping Lyman Continuum Flux at z ~1.3: Evidence for an Evolving Ionizing Emissivity. , 723(1):241–250.

Smith, A., Kannan, R., Garaldi, E., Vogelsberger, M., Pakmor, R., Springel, V., and Hernquist, L. (2022). The THESAN project: Lyman-α emission and transmission during the Epoch of Reionization. , 512(3):3243–3265.

Smith, A., Kannan, R., Tacchella, S., Vogelsberger, M., Hernquist, L., Marinacci, F., Sales, L. V., Torrey, P., Li, H., Yeh, Y.-C., and Qi, J. (2021). The physics of Lyman-alpha escape from disc-like galaxies. *arXiv e-prints*, page arXiv:2111.13721.

Smith, A., Ma, X., Bromm, V., Finkelstein, S. L., Hopkins, P. F., Faucher-Giguère, C.-A., and Kereš, D. (2019). The physics of Lyman α escape from high-redshift galaxies. , 484(1):39–59.

Smith, A., Safranek-Shrader, C., Bromm, V., and Milosavljević, M. (2015). The Lyman α signature of the first galaxies. , 449(4):4336–4362.

Springel, V. (2005). The cosmological simulation code GADGET-2. , 364(4):1105–1134.

Springel, V. (2010). E pur si muove: Galilean-invariant cosmological hydrodynamical simulations on a moving mesh. , 401(2):791–851.

Springel, V. and Hernquist, L. (2003). Cosmological smoothed particle hydrodynamics simulations: a hybrid multiphase model for star formation. , 339(2):289–311.

Springel, V., Pakmor, R., Pillepich, A., Weinberger, R., Nelson, D., Hernquist, L., Vogelsberger, M., Genel, S., Torrey, P., Marinacci, F., and Naiman, J. (2018). First results from the IllustrisTNG simulations: matter and galaxy clustering. , 475(1):676–698.

Springel, V., Yoshida, N., and White, S. D. (2001). Gadget: a code for collisionless and gasdynamical cosmological simulations. *New Astronomy*, 6(2):79–117.

Steidel, C. C., Bogosavljević, M., Shapley, A. E., Reddy, N. A., Rudie, G. C., Pettini, M., Trainor, R. F., and Strom, A. L. (2018). The Keck Lyman Continuum Spectroscopic Survey (KLCS): The Emergent Ionizing Spectrum of Galaxies at z $\sim$ 3. , 869(2):123.

Steinwandel, U. P., Moster, B. P., Naab, T., Hu, C.-Y., and Walch, S. (2020). Hot phase generation by supernovae in ISM simulations: resolution, chemistry, and thermal conduction. , 495(1):1035–1060.

Tacchella, S., Carollo, C. M., Förster Schreiber, N. M., Renzini, A., Dekel, A., Genzel, R., Lang, P., Lilly, S. J., Mancini, C., Onodera, M., Tacconi, L. J., Wuyts, S., and Zamorani, G. (2018). Dust Attenuation, Bulge Formation, and Inside-out Quenching of Star Formation in Star-forming Main Sequence Galaxies at z $\sim$ 2. , 859(1):56.

Tacchella, S., Smith, A., Kannan, R., Marinacci, F., Hernquist, L., Vogelsberger, M., Torrey, P., Sales, L., and Li, H. (2021). H-alpha emission in local galaxies: star formation, time variability and the diffuse ionized gas. *arXiv e-prints*, page arXiv:2112.00027.

Trebitsch, M., Blaizot, J., Rosdahl, J., Devriendt, J., and Slyz, A. (2017). Fluctuating feedback-regulated escape fraction of ionizing radiation in low-mass, high-redshift galaxies. , 470(1):224–239.

Trebitsch, M., Volonteri, M., Dubois, Y., and Madau, P. (2018). Escape of ionizing radiation from high-redshift dwarf galaxies: role of AGN feedback. , 478(4):5607–5625.

Trujillo, I., Chamba, N., and Knapen, J. H. (2020). A physically motivated definition for the size of galaxies in an era of ultradeep imaging. , 493(1):87–105.

Vanzella, E., Nonino, M., Cupani, G., Castellano, M., Sani, E., Mignoli, M., Calura, F., Meneghetti, M., Gilli, R., Comastri, A., Mercurio, A., Caminha, G. B., Caputi, K., Rosati, P., Grillo, C., Cristiani, S., Balestra, I., Fontana, A., and Giavalisco, M. (2018). Direct Lyman continuum and Ly α escape observed at redshift 4. , 476(1):L15–L19.

Verner, D. A., Ferland, G. J., Korista, K. T., and Yakovlev, D. G. (1996). Atomic Data for Astrophysics. II. New Analytic FITS for Photoionization Cross Sections of Atoms and Ions. , 465:487.

Vogelsberger, M., Marinacci, F., Torrey, P., and Puchwein, E. (2020a). Cosmological simulations of galaxy formation. *Nature Reviews Physics*, 2(1):42–66.

Vogelsberger, M., Nelson, D., Pillepich, A., Shen, X., Marinacci, F., Springel, V., Pakmor, R., Tacchella, S., Weinberger, R., Torrey, P., and Hernquist, L. (2020b). High-redshift JWST predictions from IllustrisTNG: dust modelling and galaxy luminosity functions. , 492(4):5167–5201.

Weinberger, R. and Hernquist, L. (2022). Modeling multi-phase gases in cosmological simulations using compressible multi-fluid hydrodynamics. *arXiv e-prints*, page arXiv:2204.05316.

Weinberger, R., Springel, V., Hernquist, L., Pillepich, A., Marinacci, F., Pakmor, R., Nelson, D., Genel, S., Vogelsberger, M., Naiman, J., and Torrey, P. (2017). Simulating galaxy formation with black hole driven thermal and kinetic feedback. , 465(3):3291–3308.

Weinberger, R., Springel, V., and Pakmor, R. (2020). The AREPO Public Code Release. , 248(2):32.

Weinberger, R., Springel, V., Pakmor, R., Nelson, D., Genel, S., Pillepich, A., Vogelsberger, M., Marinacci, F., Naiman, J., Torrey, P., and Hernquist, L. (2018). Supermassive black holes and their feedback effects in the IllustrisTNG simulation. , 479(3):4056–4072.

Weingartner, J. C. and Draine, B. T. (2001). Dust Grain-Size Distributions and Extinction in the Milky Way, Large Magellanic Cloud, and Small Magellanic Cloud. , 548(1):296–309.

Wise, J. H. (2019). Cosmic reionisation. *Contemporary Physics*, 60(2):145–163.

Wise, J. H. and Cen, R. (2009). Ionizing Photon Escape Fractions From High-Redshift Dwarf Galaxies. , 693(1):984–999.

Wise, J. H., Demchenko, V. G., Halicek, M. T., Norman, M. L., Turk, M. J., Abel, T., and Smith, B. D. (2014). The birth of a galaxy - III. Propelling reionization with the faintest galaxies. , 442(3):2560–2579.

Wu, X., Kannan, R., Marinacci, F., Vogelsberger, M., and Hernquist, L. (2019). Simulating the effect of photoheating feedback during reionization. , 488(1):419–437.

Xu, H., Wise, J. H., Norman, M. L., Ahn, K., and O'Shea, B. W. (2016). Galaxy Properties and UV Escape Fractions during the Epoch of Reionization: Results from the Renaissance Simulations. , 833(1):84.

Yajima, H., Choi, J.-H., and Nagamine, K. (2011). Escape fraction of ionizing photons from high-redshift galaxies in cosmological SPH simulations. *MNRAS*, 412(1):411–422.

Yung, L. Y. A., Somerville, R. S., Finkelstein, S. L., Popping, G., Davé, R., Venkatesan, A., Behroozi, P., and Ferguson, H. C. (2020). Semi-analytic forecasts for JWST - IV. Implications for cosmic reionization and LyC escape fraction. , 496(4):4574–4592.